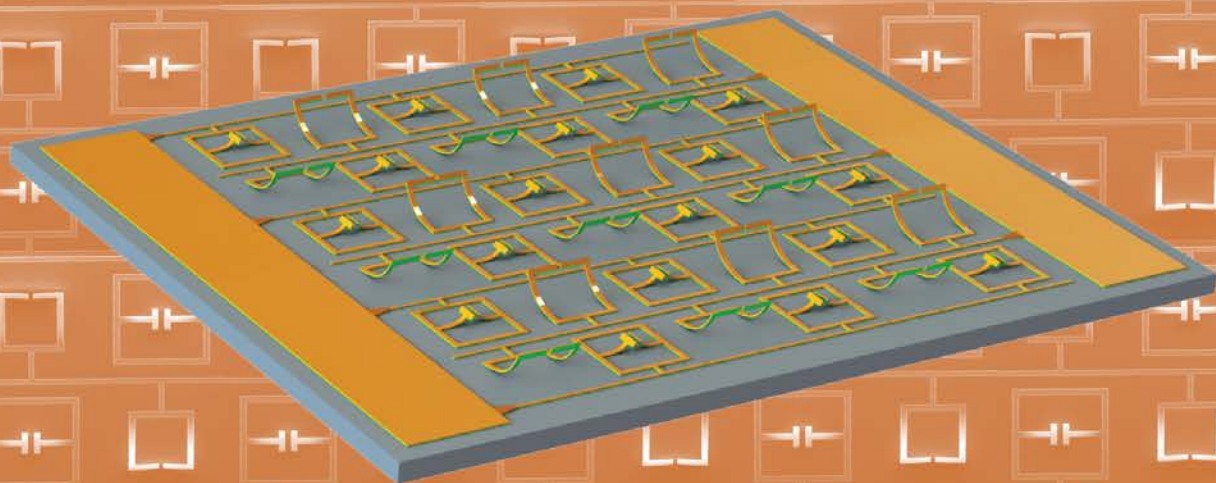


SERIES IN OPTICS AND OPTOELECTRONICS

Optical MEMS, Nanophotonics, and Their Applications



Edited by
Guangya Zhou
Chengkuo Lee

Optical MEMS, Nanophotonics, and Their Applications

SERIES IN OPTICS AND OPTOELECTRONICS

Series Editors: **Robert G W Brown**, University of California, Irvine, USA
E Roy Pike, Kings College, London, UK

Recent titles in the series

Optical MEMS, Nanophotonics, and Their Applications

Guangya Zhou and Chengkuo Lee (Eds.)

Optical Microring Resonators: Theory, Techniques, and Applications

Vien Van

Thin-Film Optical Filters, Fifth Edition

H. Angus Macleod

**Handbook of Optoelectronics, Second Edition:
Concepts, Devices, and Techniques – Volume One**

John P. Dakin and Robert Brown (Eds.)

**Handbook of Optoelectronics, Second Edition:
Enabling Technologies – Volume Two**

John P. Dakin and Robert Brown (Eds.)

**Handbook of Optoelectronics, Second Edition:
Applied Optical Electronics – Volume Three**

John P. Dakin and Robert Brown (Eds.)

Handbook of GaN Semiconductor Materials and Devices

Wengang (Wayne) Bi, Hao-chung (Henry) Kuo, Pei-Cheng Ku,
and Bo Shen (Eds.)

**Handbook of Optoelectronic Device Modeling and Simulation:
Fundamentals, Materials, Nanostructures, LEDs, and Amplifiers
– Volume One**

Joachim Piprek (Ed.)

**Handbook of Optoelectronic Device Modeling and Simulation:
Lasers, Modulators, Photodetectors, Solar Cells, and Numerical Methods
– Volume Two**

Joachim Piprek (Ed.)

Nanophotonics and Plasmonics: An Integrated View

Dr. Ching Eng (Jason) Png and Dr. Yuriy Akimov

Handbook of Solid-State Lighting and LEDs

Zhe Chuan Feng (Ed.)

Optical Compressive Imaging

Adrian Stern

Singular Optics

Gregory J. Gbur

Optical MEMS, Nanophotonics, and Their Applications

Edited by

Guangya Zhou

**Department of Mechanical Engineering,
National University of Singapore, Singapore**

and

Chengkuo Lee

**Department of Electrical and Computer Engineering,
National University of Singapore, Singapore**



CRC Press

Taylor & Francis Group

Boca Raton London New York

CRC Press is an imprint of the
Taylor & Francis Group, an **informa** business

CRC Press
Taylor & Francis Group
6000 Broken Sound Parkway NW, Suite 300
Boca Raton, FL 33487-2742

© 2018 by Taylor & Francis Group, LLC
CRC Press is an imprint of Taylor & Francis Group, an Informa business

No claim to original U.S. Government works

Printed on acid-free paper

International Standard Book Number-13: 978-1-4987-4133-0 (Hardback)

This book contains information obtained from authentic and highly regarded sources. Reasonable efforts have been made to publish reliable data and information, but the author and publisher cannot assume responsibility for the validity of all materials or the consequences of their use. The authors and publishers have attempted to trace the copyright holders of all material reproduced in this publication and apologize to copyright holders if permission to publish in this form has not been obtained. If any copyright material has not been acknowledged please write and let us know so we may rectify in any future reprint.

Except as permitted under U.S. Copyright Law, no part of this book may be reprinted, reproduced, transmitted, or utilized in any form by any electronic, mechanical, or other means, now known or hereafter invented, including photocopying, microfilming, and recording, or in any information storage or retrieval system, without written permission from the publishers.

For permission to photocopy or use material electronically from this work, please access www.copyright.com ([http://www.copyright.com/](http://www.copyright.com)) or contact the Copyright Clearance Center, Inc. (CCC), 222 Rosewood Drive, Danvers, MA 01923, 978-750-8400. CCC is a not-for-profit organization that provides licenses and registration for a variety of users. For organizations that have been granted a photocopy license by the CCC, a separate system of payment has been arranged.

Trademark Notice: Product or corporate names may be trademarks or registered trademarks, and are used only for identification and explanation without intent to infringe.

Visit the Taylor & Francis Web site at
<http://www.taylorandfrancis.com>

and the CRC Press Web site at
<http://www.crcpress.com>

Contents

Series preface	vii
Preface	ix
Editors	xi
Contributors	xiii

SECTION I Optical MEMS for communication, imaging, and sensing applications

1 Optical MEMS: An introduction	3
<i>Guangya Zhou and Chengkuo Lee</i>	
2 MEMS optical scanners for laser projection display	39
<i>Hiroshi Toshiyoshi</i>	
3 Optical micro-electrical-mechanical phased array	59
<i>Youmin Wang and Ming-Chiang Wu</i>	
4 Optical MEMS for space: Design, characterization, and applications	79
<i>Frederic Zamkotsian</i>	
5 MEMS vibratory grating scanners and their applications	115
<i>Guangya Zhou</i>	
6 F–P filters and applications in spectrometers and gas sensing	133
<i>Chong Pei Ho and Chengkuo Lee</i>	
7 Electrothermally actuated MEMS mirrors: Design, modeling, and applications	159
<i>Huikai Xie, Xiaoyang Zhang, Liang Zhou, and Sagnik Pal</i>	
8 MEMS tunable optics: Liquid and solid methods	187
<i>Yongchao Zou and Guangya Zhou</i>	

SECTION II Nanophotonics for communication, imaging, and sensing applications

9 Physical sensors based on photonic crystals	217
<i>Bo Li and Chengkuo Lee</i>	
10 Silicon photonic variable waveguide coupler devices	253
<i>Kazuhiro Hane</i>	

11	Metasurface and ultrathin optical devices	281
	<i>Xianzhong Chen, Dandan Wen, and Fuyong Yue</i>	
12	Optical micro- and nanoresonators for biochemical sensing	301
	<i>Xingwang Zhang, Liying Liu, Lei Xu, Xudong Fan, and Guangya Zhou</i>	
13	Terahertz MEMS metamaterials	321
	<i>Prakash Pitchappa and Chengkuo Lee</i>	
SECTION III Biomicro- and nanophotonics and optofluidics for health care applications		
14	Optofluidic devices and their applications	347
	<i>Sung-Yong Park</i>	
15	Implantable CMOS microphotonic devices	377
	<i>Jun Ohta and Takashi Tokuda</i>	
16	Microfluidic photocatalysis	403
	<i>Ning Wang and Xuming Zhang</i>	
	Index	425

Series preface

This international series covers all aspects of theoretical and applied optics and optoelectronics. Active since 1986, eminent authors have long been choosing to publish with this series, and it is now established as a premier forum for high-impact monographs and textbooks. The editors are proud of the breadth and depth showcased by published works, with levels ranging from advanced undergraduate and graduate student texts to professional references. Topics addressed are both cutting edge and fundamental, basic science and applications-oriented, on subject matter that includes: lasers, photonic devices, nonlinear optics, interferometry, waves, crystals, optical materials, biomedical optics, optical tweezers, optical metrology, solid-state lighting, nanophotonics, and silicon photonics. Readers of the series are students, scientists, and engineers working in optics, optoelectronics, and related fields in the industry.

Proposals for new volumes in the series may be directed to Lu Han, executive editor at CRC Press, Taylor & Francis Group (lu.han@taylorandfrancis.com).



Taylor & Francis

Taylor & Francis Group

<http://taylorandfrancis.com>

Preface

Microelectromechanical systems (MEMS) technology, which features integration and miniaturization of mechanical and electrical elements at the microscale using IC-like microfabrication processes, is now well-known and has already had a profound impact on a range of engineering and scientific fields. Optical MEMS that involve the use of MEMS devices in optical and photonic systems to dynamically manipulate the light have been rapidly developed in the past decades. Optical MEMS technology not only provides the advantages of system miniaturization, performance enhancement, and low cost production, but also enables new applications and innovations. Examples include micromirrors for portable displays, ultra-compact endoscopic probes, and micromirror arrays for ground- and space-based telescopes. Some of these optical MEMS-based devices and systems are already commercially available on the market.

More recently, as the nanofabrication technology has made significant progress, further scaling of MEMS down to nanoelectromechanical systems (NEMS) is now possible. At the same time, research in nanophotonics that focuses on the interaction of light with engineered nanostructures has gained significant momentum. In our view, the fusion of MEMS/NEMS with nanophotonic elements also opens up new possibilities and creates novel functional photonic devices and systems featuring dynamic tunability, enhanced performance, and a higher level of integration. Fascinating new devices, systems, and applications, for example, NEMS-driven variable silicon nanowire waveguide couplers and NEMS tunable photonic crystal (PhC) nanocavities, are emerging at a fast pace.

This edited book describes some of the most recent results in the field of optical MEMS and nanophotonics. It is challenging to provide a complete reference to address the rapid developments in this area, since new devices, systems, and applications are reported all the time. It is our intention to provide the engineers and researchers who are interested in micro- and nanofabrication, MEMS/NEMS, micro-optics, and nanophotonics the necessary fundamentals in this field as well as a source of information on recent photonic NEMS/MEMS devices and their uses.

This book aims to cover a broad spectrum and is divided into three sections. The first section addresses typical optical MEMS devices containing micro-sized features. It also features the use of this technology in imaging, communication, and sensing applications. This section presents a set of devices and systems, including PZT-driven micromirrors for ultra-portable laser scanning project displays, optical phased array technology using MEMS-driven high-contrast-grating (HCG) mirrors for fast beam steering, electrostatically driven programmable mirror arrays for space instruments, ultra-fast laser scanning using MEMS-driven vibratory gratings and their applications in hyperspectral imaging, MEMS-based tunable Fabry–Pérot filters, electrothermally driven micromirrors and their applications in endoscopes, and MEMS-driven tunable lenses and adjustable apertures for miniaturized cameras. The second section of the book covers the recent research in nanophotonics, again with an emphasis on its integration with NEMS/MEMS. This section reports on photonic crystal-based sensors, NEMS-driven silicon nanowire waveguide variable couplers, metasurfaces and ultrathin optical devices, sensors based on nanophotonic resonators, and MEMS tunable THz metamaterials. The last section of the book presents particular types of micro- and nanophotonic devices that integrate with biological and/or microfluidic systems. This section reports on microfluidic devices and their applications, implantable microphotonic devices, as well as

portable microfluidic-based photocatalysis systems. These devices and systems are mostly targeted for biomedical and health care applications.

Last but not least, we wish to thank all the authors who contributed to this book. Their fascinating contributions, suggestions, and commitment made this book possible.

Guangya Zhou
Chengkuo Lee
Singapore

Guangya Zhou received his B.Eng. and PhD degrees in optical engineering from Zhejiang University, Hangzhou, China, in 1992 and 1997, respectively. His PhD thesis was on micro-optics and diffractive optics. He was a post-doctoral fellow at State Key Laboratory of thin film and microfabrication technology at Shanghai Jiao Tong University from 1997 to 1999, conducting research on optical MEMS for telecommunication systems. In 2000, he joined the School of Electrical and Electronic Engineering at Nanyang Technological University as a research fellow, where his research was on III-V semiconductor-based optical MEMS devices. He joined the Department of Mechanical Engineering, National University of Singapore in 2001 as a research fellow and in 2005 as an assistant professor. Since 2012, he has been an associate professor in the same department. His research covers optical MEMS scanners, MEMS spectrometers and hyperspectral imagers, optical MEMS-based ultra-compact endoscope probes, silicon nanophotonics, NEMS tunable photonic crystals, and nanoscale optomechanics. He has published over 100 research papers in peer-reviewed international journals in the fields of micro-optics, nanophotonics, micro-/nanofabrication, MEMS, and NEMS. He is the main inventor of the MEMS-driven vibratory grating scanner, MEMS-based miniature zoom lens system with autofocus function, and miniature MEMS-based adjustable aperture. The latter two were successfully licensed to a start-up company, where he currently also works as a technical advisor.

Chengkuo Lee received his MS degree in materials science and engineering from National Tsing Hua University, Hsinchu, Taiwan, in 1991, his M.S. degree in industrial and system engineering from Rutgers University, New Brunswick, NJ, in 1993, and his PhD in precision engineering from The University of Tokyo, Tokyo, Japan, in 1996. He was a Foreign Researcher with the Nanometer-Scale Manufacturing Science Laboratory of the Research Center for Advanced Science and Technology, The University of Tokyo, from 1993 to 1996. He was with the Mechanical Engineering Laboratory, AIST, MITI of Japan, as a JST Research Fellow, in 1996. Thereafter, he became a Senior Research Staff Member of the Microsystems Laboratory, Industrial Technology Research Institute, Hsinchu. In 1997, he joined Metrodyne Microsystem Corporation, Hsinchu, and established the MEMS Device Division and the first micromachining lab for commercial purposes in Taiwan. He was the Manager of the MEMS Device Division between 1997 and 2000. He was an Adjunct Assistant Professor with the Electro-Physics Department, National Chiao Tung University, Hsinchu, in 1998, and an Adjunct Assistant Professor with the Institute of Precision Engineering, National Chung Hsing University, Taichung, Taiwan, from 2001 to 2005. In 2001, he cofounded Asia Pacific Microsystems, Inc., Hsinchu, where he first became Vice President of Research and Development, before becoming Vice President of the Optical Communication Business Unit and Special Assistant to the Chief Executive Officer in charge of international business and technical marketing for the MEMS foundry service. He was a Senior Member of the Technical Staff at the Institute of Microelectronics, A*STAR, Singapore, from 2006 to 2009. Currently, he is an Associate Professor with the Department of Electrical and Computer Engineering, National University of Singapore, Singapore. He is the co-author of *Advanced MEMS Packaging* (McGraw-Hill, 2010). He has contributed to more than 230 international conference papers and extended abstracts and 160 peer-reviewed international journal articles in the fields of optical MEMS, NEMS, nanophotonics, and nanotechnology. He holds nine U.S. patents.



Taylor & Francis

Taylor & Francis Group

<http://taylorandfrancis.com>

Contributors

Xianzhong Chen

Institute of Photonics and Quantum Sciences
School of Engineering and Physical Sciences
Heriot-Watt University
Edinburgh, Scotland, United Kingdom

Xudong Fan

Department of Biomedical Engineering
University of Michigan
Ann Arbor, Michigan

Kazuhiro Hane

Tohoku University
Sendai, Japan

Chong Pei Ho

Department of Electrical and Computer
Engineering
National University of Singapore
Singapore

Bo Li

Department of Electrical and Computer
Engineering
National University of Singapore
Singapore

Liyang Liu

Department of Optical Science and
Engineering
School of Information Science and
Engineering
Fudan University
Shanghai, China

Jun Ohta

Graduate School of Materials Science
Nara Institute of Science and Technology
Ikoma, Japan

Sagnik Pal

Department of Electrical and Computer
Engineering
University of Florida
Gainesville, Florida

Sung-Yong Park

Department of Mechanical Engineering
National University of Singapore
Singapore

Prakash Pitchappa

Department of Electrical and Computer
Engineering
National University of Singapore
Singapore

Takashi Tokuda

Graduate School of Materials Science
Nara Institute of Science and Technology
Ikoma, Japan

Hiroshi Toshiyoshi

Research Center for Advanced Science and
Technology
The University of Tokyo
Tokyo, Japan

Ning Wang

National Engineering Laboratory for Fiber
Optic Sensing Technology
Wuhan University of Technology
Wuhan, People's Republic of China

Youmin Wang

Department of Electrical Engineering and
Computer Sciences
University of California, Berkeley
Berkeley, California

Dandan Wen

Institute of Photonics and Quantum Sciences
School of Engineering and Physical Sciences
Heriot-Watt University
Edinburgh, Scotland, United Kingdom

Ming-Chiang Wu

Department of Electrical Engineering and
Computer Sciences
University of California, Berkeley
Berkeley, California

Huikai Xie

Department of Electrical and Computer
Engineering
University of Florida
Gainesville, Florida

Lei Xu

Department of Optical Science and
Engineering
School of Information Science and Engineering
Fudan University
Shanghai, People's Republic of China

Fuyong Yue

Institute of Photonics and Quantum Sciences
School of Engineering and Physical Sciences
Heriot-Watt University
Edinburgh, Scotland, United Kingdom

Frederic Zamkotsian

Laboratoire d'Astrophysique de
Marseille (LAM)
French National Research (CNRS) and
Aix Marseille Univ
Marseille, France

Xiaoyang Zhang

Department of Electrical and
Computer Engineering
University of Florida
Gainesville, Florida

Xingwang Zhang

Department of Mechanical Engineering
National University of Singapore
Singapore

Xuming Zhang

Department of Applied Physics
Hong Kong Polytechnic University
Hong Kong, People's Republic of China

Liang Zhou

Department of Electrical and Computer
Engineering
University of Florida
Gainesville, Florida

Yongchao Zou

Department of Mechanical Engineering
National University of Singapore
Singapore

SECTION I

Optical MEMS for communication,
imaging, and sensing applications



Taylor & Francis

Taylor & Francis Group

<http://taylorandfrancis.com>

Optical MEMS: An introduction

Guangya Zhou and Chengkuo Lee

Contents

1.1	MEMS processes	3
1.1.1	Lithography	4
1.1.2	Thin film formation	5
1.1.3	Etching	6
1.1.4	Bonding	8
1.2	Actuation schemes	9
1.2.1	Electrothermal actuation	9
1.2.2	Electrostatic actuation	11
1.2.3	Piezoelectric actuation	13
1.2.4	Electromagnetic actuation	15
1.3	Optical MEMS for imaging	16
1.4	Optical MEMS for displays	18
1.4.1	Scanning-based MEMS displays: Point source 2D scanning	19
1.4.2	Scanning-based MEMS displays: Linear array 1D scanning	20
1.4.3	Non-scanning-based MEMS displays	21
1.5	Optical MEMS for sensing	23
1.5.1	Noncoherent optical MEMS sensors	23
1.5.2	Coherent optical MEMS sensors	24
1.5.2.1	Optical MEMS sensors based on Michelson interferometers	25
1.5.2.2	Optical MEMS sensors based on lamellar grating interferometers	26
1.5.2.3	Optical MEMS sensors based on Fabry–Pérot interferometers	28
1.6	Conclusions	30
	References	30

1.1 MEMS processes

Fabrication of devices in micro-/nanometer scales requires microelectromechanical systems (MEMS) technology which allows for static or moveable elements for sensing and actuation purposes. This chapter provides an overview of the basic MEMS fabrication methods. Developed from the modern complementary metal-oxide-semiconductor (CMOS) process, MEMS enables the integration of different functions with electronic circuits, thus is a key technology for the fabrication of future devices. A standard MEMS fabrication process includes lithography, thin-film formation, etching, and bonding and packaging. Various materials such as silicon, polymers,

metals, and ceramics are used and must be processed in micro-/nanometer scale. The following section describes the fundamental MEMS process steps in detail.

1.1.1 Lithography

Photolithography is widely used for micro-/nanometer sized patterning. A mask, which contains the desired pattern layer on a glass plate, is required in the process. Typically, a glass mask is fabricated with an electron beam lithography technique where a computer-aided design (CAD) can be written on a glass plate with a metal layer (typically chromium) followed by an etching process to form the pattern layer [1]. Figure 1.1 illustrates the standard photolithographic process to transfer the desired pattern onto a thin film on a substrate. First, a photosensitive material (photoresist) is coated on the thin film. Next, the mask with the desired pattern is brought into contact or close to contact and aligned with the substrate using a mask aligner. This step ensures that the pattern is exposed at the correct location for the subsequent fabrication steps. The photoresist is then exposed to ultraviolet (UV) light through the glass mask layer. There are two types of photoresist, positive and negative. For a positive photoresist, the exposed part is more soluble in the developing solution hence it is removed in the development. On the other hand, a negative photoresist is polymerized through exposure and becomes difficult to dissolve, hence the exposed part remains on the substrate after development. After the development, the remaining photoresist acts as a protective layer in the pattern transfer process. Finally, the photoresist is stripped out leaving the thin film with the desired pattern on the substrate.

Recently, nanoimprint lithography (NIL) has been studied and introduced as a patterning method in MEMS technology. A mold is required in the patterning process, which acts as a stamp and contains the desired pattern. NIL can be categorized into thermal NIL, UV NIL, and Soft NIL. Figure 1.2 illustrates the standard process of thermal and UV NIL. First, a layer of polymer is applied on top of the substrate. The polymer is designed to cure through application of heat or exposure to UV light. Second, the mold is in contact and is pressed to the substrate which is coated with the curable polymer. Heat is provided for the curing of the polymer in the case of

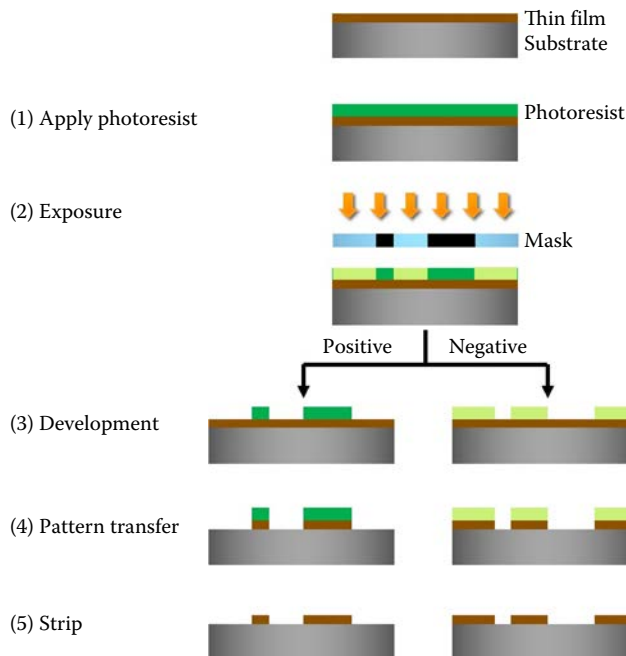


Figure 1.1 Schematic illustration of photolithographic process sequence for pattern transfer.

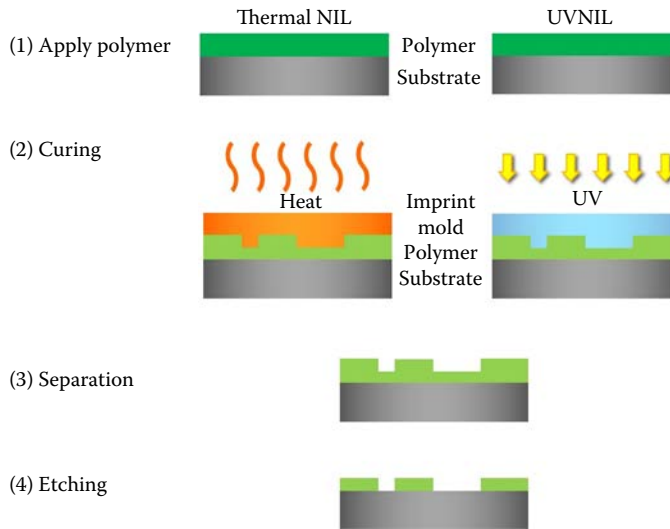


Figure 1.2 Schematic illustration of nanoimprint lithography (NIL) process sequence.

thermal NIL, while UV light is provided to cure the polymer for UV NIL. The substrate or the mold material needs to be transparent to UV light when adapting to the UV NIL process. After curing, the mold is separated from the substrate and the residual polymer at the bottom is etched away. The NIL process is especially unique in soft NIL where the mold is made from a soft material such as poly(dimethylsiloxane) (PDMS). This soft mold enables large area patterning using methods such as roll-to-sheet or roll-to-roll imprinting.

1.1.2 Thin film formation

The deposition method of the thin film in MEMS can be categorized as physical vapor deposition (PVD) or chemical vapor deposition (CVD). PVD use a physical method such as vaporizing or using ion bombardment of the targeted material and forcing it to turn into the gaseous phase. The gaseous phase source is then deposited as a thin-film on a substrate. On the other hand, CVD creates a thin film through a chemical reaction on the substrate surface. The most common PVD method is thermal evaporation as shown in Figure 1.3a. Heat is provided to melt the source material which turns into the liquid phase and eventually evaporates in the vacuum chamber. The vaporized source material then travels through the chamber to the substrate, thus forming a thin-film on the

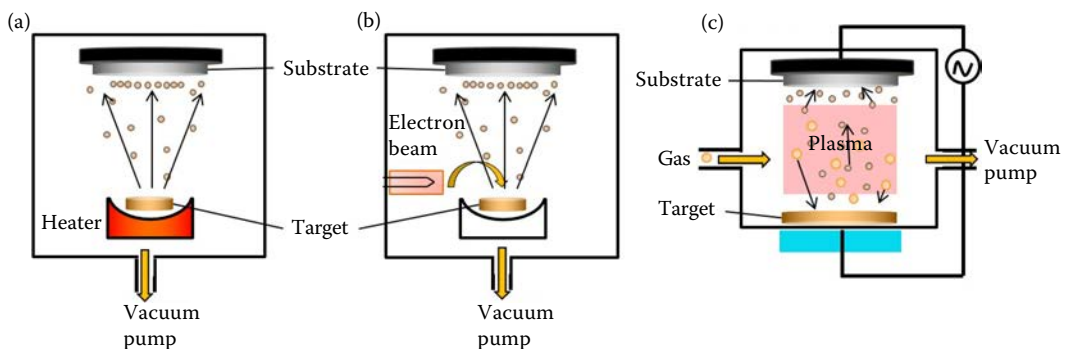


Figure 1.3 Schematic illustration of major physical vapor deposition (PVD): (a) thermal evaporation, (b) electron beam (E-beam) evaporation, and (c) sputtering.

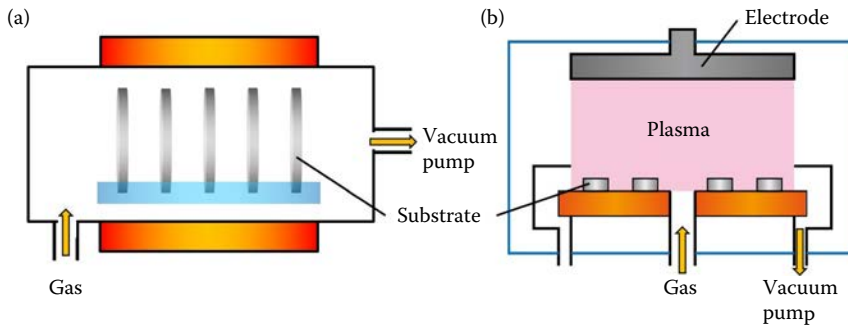


Figure 1.4 Schematic illustration of major physical vapor deposition (PVD). (a) Low pressure CVD (LPCVD), (b) plasma-enhanced CVD (PECVD).

surface. The heat can be provided by introducing current into the conductive supporting material which has a high melting point. Hence, by putting the target source material on top, thermal evaporation can be achieved. While these supporting materials allow evaporation, they may lead to contamination in the chamber. Electron beam (E-beam) evaporation is a method similar to thermal evaporation, but with a different melting method. As illustrated in [Figure 1.3b](#), an electron gun is used to provide high energy for melting the target source material. This minimizes the possibility of contamination from supporting materials while also allowing finer control of the deposition rate. Plasma is also used as a method to directly turn the solid target into atoms, thus forming a thin film on the substrate. This process is called sputtering. [Figure 1.3c](#) shows the schematic of the AC sputtering process. A gas source is introduced into the vacuum chamber where AC voltage is applied between the top and bottom electrodes, which generates plasma. An ion bombardment process occurs, thus the target source material is physically etched away from the surface. These atoms are then deposited on the substrate to create a thin film.

The chemical vapor deposition (CVD) process also takes place in a chamber where the substrates are placed in a holder. Reactive gases are introduced into the chamber and form a thin film on the substrate surface. The produced by-product then exits the chamber. Due to this film-forming mechanism, both the reactive chemicals and the by-product in the CVD process need to be volatile while creating a non-volatile solid film. The energy for the reaction is supplied by thermal methods, photons, or electrons. The advantage of CVD over PVD is its high deposition rate and good step coverage. CVD can be conducted in atmospheric pressure and in reduced pressures. However, a lower chamber pressure allows better control in the deposition rate while also reducing the contamination. [Figure 1.4a](#) illustrates low-pressure CVD (LPCVD) which is operated in reduced pressure and allows for batch processing. The heater around the chamber provides the thermal energy for the chemical reaction. Plasma can also be an energy source for the chemical reaction. This system is called plasma-enhanced CVD (PECVD) as illustrated in [Figure 1.4b](#). The gases in the chamber are highly reactive due to the plasma created by the applied bias. This allows for film formation on the substrates placed in the chamber. PECVD allows for film deposition with a high rate but at lower temperatures compared to LPCVD.

1.1.3 Etching

The deposited thin film can be partially removed in a desired pattern through the etching process. The etching process can be categorized into a wet process and a dry process. While the etchant of wet etching is in the liquid state, the etchant for dry etching is usually in a gas or plasma state. Wet etching can be conducted by immersing the substrate into the etchant liquid or spraying the etchant on the substrate. The etchant will then react with the substrate material creating a by-product to be washed away. Wet etching has the advantages of a high etching rate and high selectivity over the

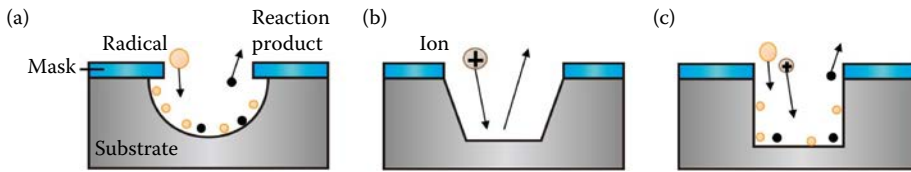


Figure 1.5 Schematic illustration of etching mechanisms: (a) chemical etching, (b) physical etching, (c) reactive ion etching (RIE).

selected mask layer, while the etching is not directional. Hence, it is mostly used for structure releasing in the MEMS process. On the other hand, dry etching is more commonly used in the etching of the actual structure in MEMS utilizing the etchant in the form of a plasma. In chemical dry etching, gaseous etchants encounter collisions with charged particles, resulting in a dissociation and excitation [2]. These reactive molecules then etch away the substrate materials. The physical dry etching process is similar to the sputtering process for thin-film deposition. The reactive ions bombard the substrates and etch away the material. A commonly used method in dry etching is reactive ion etching (RIE), where both chemical and physical etching take place as illustrated in Figure 1.5c.

There are two main types of process set ups for RIE, capacitive coupled plasma (CCP) RIE and inductive coupled plasma (ICP) RIE. As illustrated in Figure 1.6a, CCP-RIE contains two parallel electrodes in a side vacuum chamber. RF bias is through a blocking capacitor to the bottom electrode where the substrate to be etched is placed. Gas is fed into the vacuum chamber and plasma is generated. The plasma is then driven to the substrate surface and etches the material. The ICP system contains two bias generators, one of which controls the plasma density while the other controls the ion energy (Figure 1.6b). The induction coil at the top of the vacuum chamber generates plasma above the substrate and hence provides better control of the plasma density while also allowing higher plasma density for the CCP system. The other bias is provided to the bottom electrode which drives plasma to the substrate surface and hence controls the ion energy for the etching process.

Deep reactive ion etching (DRIE) is known as a process for Si etching with vertical side walls and a high aspect ratio. It was invented by Larmer and Urban at Robert Bosch Corporate Research [3], thus the process is often called the Bosch process. The Bosch process requires switching between several gases in the ICP-RIE set up, thus an ICP-RIE machine with the capability to program and switch gases is called a DRIE. Figure 1.7 depicts the process steps in the Bosch process. Starting from an Si with a masking layer and an exposed area to etch, sulfur hexafluoride (SF_6)-based etching gas is first introduced into the chamber. In the SF_6 plasma, ions contribute to directional physical etching while the fluorine radicals contribute to isotropic chemical etching. The gas in the chamber is then switched to octafluorocyclobutane (C_4F_8) which forms a passivation fluorocarbon layer on the

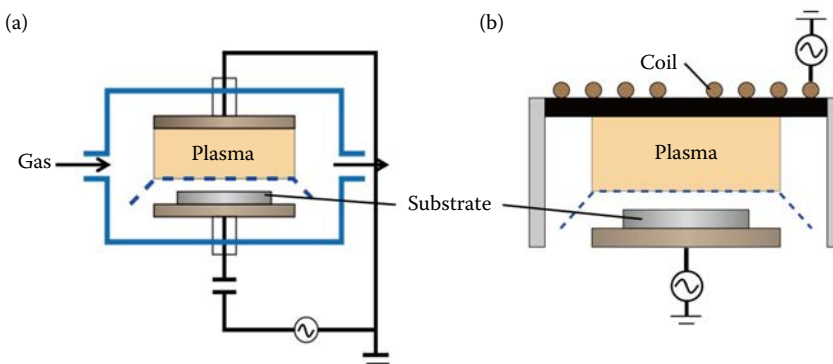


Figure 1.6 Schematic illustration of a major reactive ion etching (RIE) system: (a) capacitive coupled plasma (CCP) RIE, (b) inductive coupled plasma (ICP) RIE.

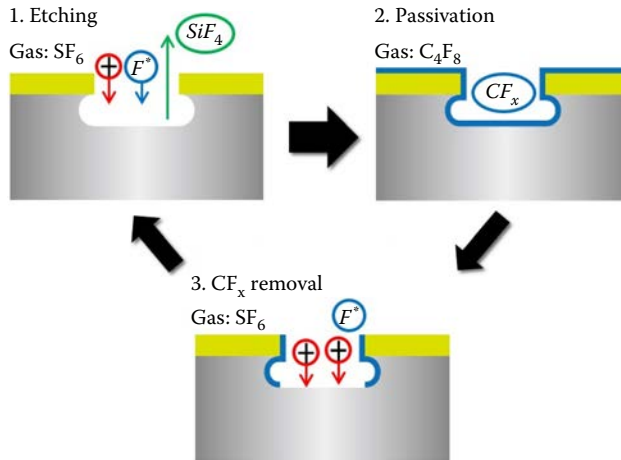


Figure 1.7 Schematic illustration of the etching steps of the Bosch process for high aspect ratio etching.

whole surface. After the passivation process, the gas is switched back to SF_6 , but with bias control to enhance the ion bombardment effect of the SF_6 plasma. This allows for the removal of the passivation layer at the bottom of the etched silicon. The process then returns back to the first etching condition to conduct another Si etching. The remaining passivation layer on the side wall functions as a protective layer in the etching process, thus the side wall remains vertical. The process then passes to step three in [Figure 1.7](#) and is repeated in cycles until the desired depth is achieved.

1.1.4 Bonding

A bonding technique is necessary for MEMS devices that require sealing or consist of multiple layers of wafer. This chapter covers direct wafer bonding and anodic bonding. Direct wafer bonding is also called silicon to silicon fusion bonding and applies a high temperature to both wafers [4]. The surfaces to be bonded need to be cleaned and smoothed enough to ensure firm contact between the two wafers. Surface activation is required in direct bonding where the wafer surface is chemically activated. This can be done through immersing the wafer into ammonium hydroxide (NH_4OH) or by exposure to oxygen (O_2) plasma [2]. The wafers are then brought into contact at room temperature. The temperature is then increased to (typically) 1100°C which results in strong siloxane Si-O-Si bonds between the two silicon wafers. Anodic bonding is a bonding method for glass and silicon bonding. The temperature for this process is lower than that of silicon to silicon fusion bonding, typically $300\text{--}500^\circ\text{C}$, where an electrical DC voltage is applied across both wafers as illustrated in [Figure 1.8](#). Glass is mainly composed of silica, and many silica-based glasses

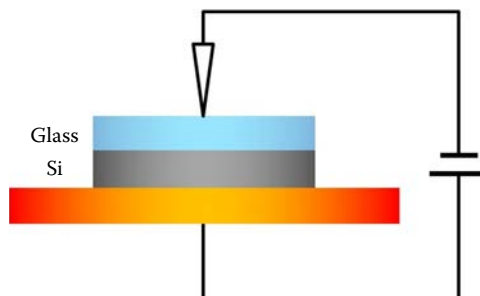


Figure 1.8 Schematic illustration of the anodic bonding.

contain ions such as sodium oxide (Na_2O) or calcium oxide (CaO). The DC voltage drives these ions to the cathode side while leaving negative ions in the glass–silicon boundary. A direct siloxane (Si-O-Si) bond is then formed between the glass and silicon.

1.2 Actuation schemes

Recent developments in the rapidly emerging discipline of MEMS have shown immense promise in actuators and micro-optical systems [1]. In conjunction with properly designed mirrors, lenses, and gratings, various micro-optical systems driven by microactuators can provide many unique functions in light manipulation such as reflection, beam steering, filtering, focusing, collimating, diffracting, etc. In the next few sections, the four major actuation schemes, that is, electrothermal, electrostatic, piezoelectric, and electromagnetic, for in-plane or out-of-plane movements, are introduced. Each actuation scheme has its inherent advantages and disadvantages, while its design feasibilities are often limited by the fabrication method used.

1.2.1 Electrothermal actuation

Electrothermal actuation makes use of the difference in the thermal expansions of materials to achieve mechanical actuation. The thermal expansion of a solid material is characterized by the coefficient of thermal expansion (CTE), αT , and has a unit of strain per change in temperature (K^{-1}). With a small temperature change of ΔT , the introduced mechanical strain ε is defined as the product,

$$\varepsilon = \alpha T \cdot \Delta T \quad (1.1)$$

One of the basic actuator structures for thermal actuation, as shown in [Figure 1.9](#), is an electrothermal bimorph that consists of a cantilever with two different material layers [2–5]. The actuation relies on the difference in the linear expansion coefficients of the two materials, with one layer expanding by a larger amount than the other. This results in stress at the interface of these two layers, leading to bending of the cantilever. The elevated temperature can be created by heating up the cantilever when a bias current flows through an embedded resistor

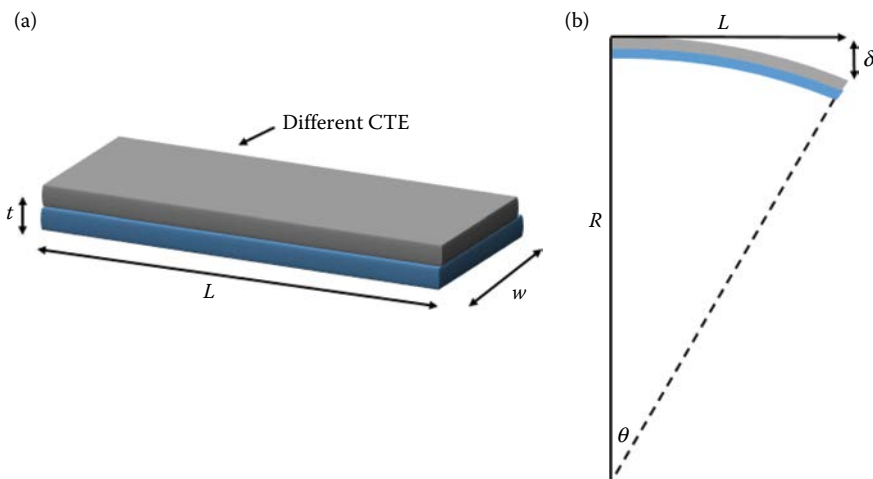


Figure 1.9 Schematic illustration of electrothermal bimorph: (a) material composition and (b) vertical displacement δ .

in the cantilever, which is the Joule heating effect. The radius of bending curve R and vertical displacement are

$$\delta = R - R\cos\theta \cong R - R\left(1 - \frac{1}{2}\theta^2\right) = \frac{L^2}{2R} \quad (1.2)$$

$$\frac{1}{R} = \frac{6w_1w_2E_1E_2t_1t_2(t_1+t_2)(\alpha_1-\alpha_2)\Delta T}{(w_1E_1t_1^2)^2 + (w_2E_2t_2^2)^2 + 2w_1w_2E_1E_2t_1t_2(2t_1^2 + 2t_2^2 + 3t_1t_2)} \quad (1.3)$$

where α_1 , α_2 , w_1 , w_2 , E_1 , E_2 , t_1 , and t_2 are CTE, width, Young's modulus, and thickness of the two layers, respectively. Thus, the δ can be rewritten into another form [6],

$$\delta = \frac{3w_1w_2E_1E_2t_1t_2(t_1+t_2)(\alpha_1-\alpha_2)\Delta TL^2}{(w_1E_1t_1^2)^2 + (w_2E_2t_2^2)^2 + 2w_1w_2E_1E_2t_1t_2(2t_1^2 + 2t_2^2 + 3t_1t_2)} \quad (1.4)$$

L is the length of the bimorph. The equivalent stiffness EI for the bimorph is

$$EI = \frac{w_2^3t_1E_1E_2}{12(E_1t_1 + E_2t_2)} K \quad (1.5)$$

$$K = \left[4 + 6\frac{t_1}{t_2} + 4\left(\frac{t_1}{t_2}\right)^2 + \frac{E_1}{E_2}\left(\frac{t_1}{t_2}\right)^3 + \frac{E_2t_2}{E_1t_1} \right] \quad (1.6)$$

The total force generated at the free end of the bimorph due to thermally induced deflection is

$$F = \frac{3EI}{L^3} \frac{3\Delta\alpha\Delta T \left(1 + \frac{t_1}{t_2}\right) L^2}{t_2 \left\{ \left(\frac{w_1}{w_2} \frac{E_1}{E_2}\right) \left(\frac{t_1}{t_2}\right)^3 + \left(\frac{w_2}{w_1} \frac{E_2}{E_1}\right) \left(\frac{t_2}{t_1}\right) + 2 \left[2\left(\frac{t_1}{t_2}\right)^2 + 3\left(\frac{t_1}{t_2}\right) + 2 \right] \right\}} \quad (1.7)$$

In addition to out-of-plane actuation, there are other applications demanding in-plane displacement, which will involve designs that are different from the above-mentioned bimorph actuator. For example, in-plane actuation is made possible by designing a U-shaped electrothermal actuator consisting of two arms of uneven widths [7] from a single material. As shown in [Figure 1.10a](#), when an electrical current is applied from one anchor to the other, the arm with the larger electrical resistance heats up more. This results in a higher temperature and larger volume expansion in the thinner arm, that is, the so-called hot arm. The other thicker arm is relatively cold and is referred to as the cold arm. Eventually, the U-shaped thermal actuator will deflect laterally toward the cold arm side due to asymmetrical thermal expansion when the actuator is DC biased. Other variations of the classical single hot-cold arms design have also surfaced, with some research groups focusing on two hot arms and one cold arm design [8–10], and one group having integrated a piezoresistive lateral displacement sensor embedded into the actuator [11]. Other designs for in-plane electrothermal actuators, such as V-shaped chevron beam actuators illustrated in [Figure 1.10b](#), have also been reported [12–14].

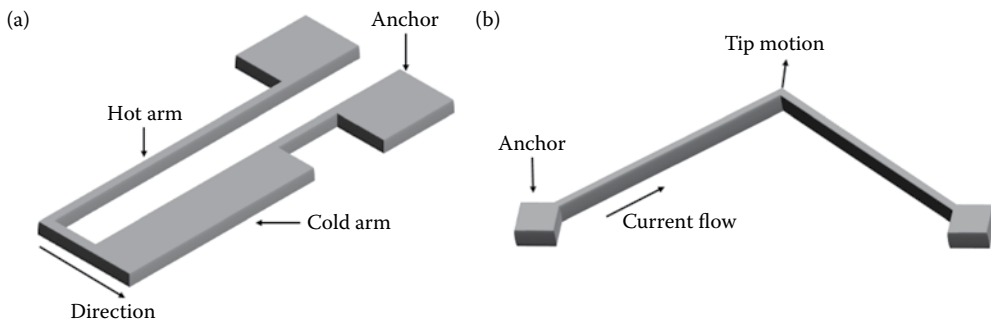


Figure 1.10 Schematic diagram of (a) in-plane U-shaped actuator, which deploys hot-cold arms of different width and (b) in-plane V-shaped chevron beam actuator that buckles along tip when current flows through.

Compared to other actuation schemes, an electrothermal actuator can achieve large forces ($\sim 100 \mu\text{N}$) and static displacements ($\sim 100 \mu\text{m}$) at relatively low voltages ($\sim 5 \text{ V}$) [1]. However, a large amount of thermal energy is required, therefore, it consumes substantial electrical energy ($\sim 1 \text{ W}$). In addition, it has a slower response and AC operation of the thermal actuator is generally limited to a frequency response of less than 1 kHz. This is due to the time constant associated with heat transfer. High temperature and complicated thermal management are further drawbacks of thermal actuation. For example, the upper practical limits for temperatures in polysilicon and single-crystal-silicon-based electrothermal actuator are approximately 600°C and 800°C , respectively, above which material property changes such as localized plastic yielding and material grain growth become an issue.

1.2.2 Electrostatic actuation

There are two major types of electrodes that are commonly used for electrostatic actuation: parallel plates [15,16] and interdigitated combs as illustrated in Figures 1.11 and 1.12. A typical configuration usually consists of a movable electrode connected to suspended mechanical springs while a fixed electrode is anchored onto the substrate. When a voltage is applied to the capacitive electrodes, the electrostatic attractive force actuates the movable electrode to the stationary electrode, causing the area of overlap and the capacitance between the two electrodes to increase. As a result, the spring suspending the movable electrode is deformed. Thus, the force balance between the spring restoring force and the electrostatic force determines the displacement of the movable

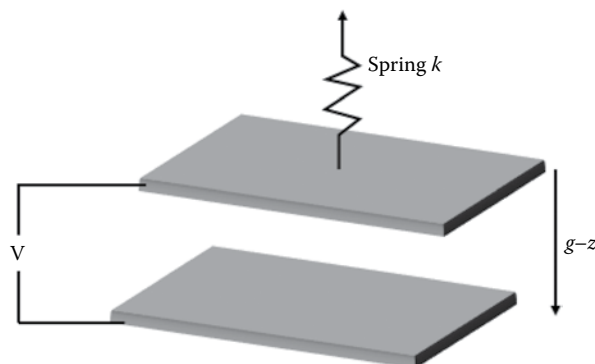


Figure 1.11 Parallel plates with applied voltage as electrostatic actuator; g is gap and z is displacement.

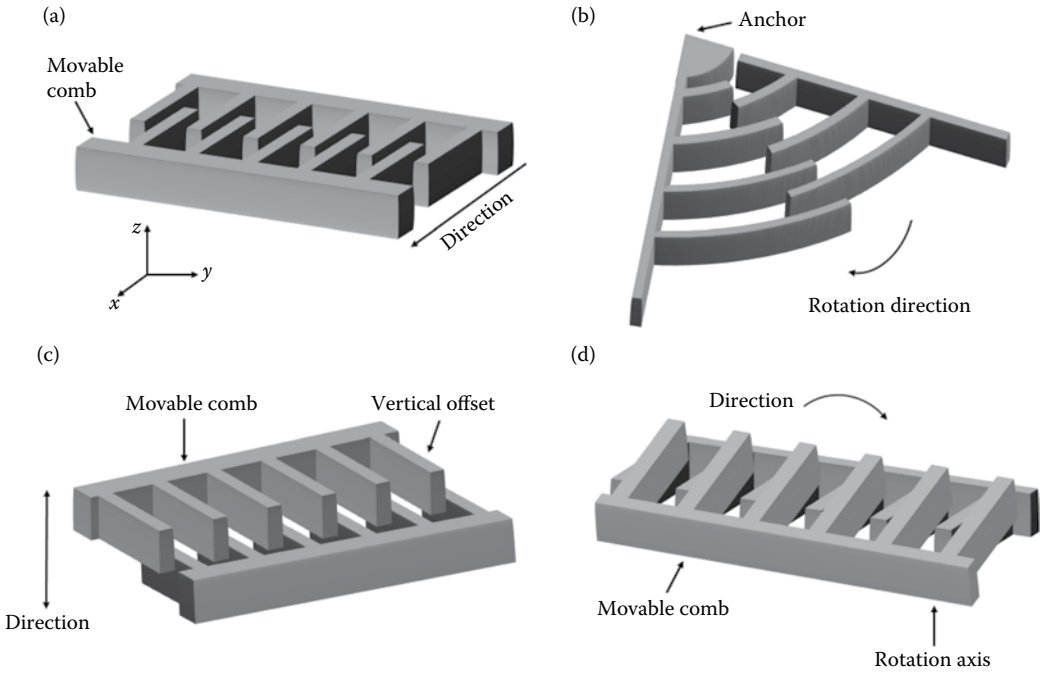


Figure 1.12 Schematic diagram illustrating the various types of electrostatic actuators commonly adopted in literature. They are (a) in-plane parallel lateral comb, (b) in-plane rotary combs, because of symmetrical structure only a part is drawn here, (c) out-of-plane staggered vertical combs, and (d) out-of-plane angular vertical combs.

electrode. Ignoring fringing effects, the force at a certain voltage V can be given by considering the energy stored inside the parallel plates W ,

$$W = \frac{1}{2} \frac{\epsilon A}{g - z} V^2 \tag{1.8}$$

$$\frac{\partial W}{\partial z} = F = \frac{1}{2} \frac{\epsilon A}{(g - z)^2} V^2 \tag{1.9}$$

where g is the gap length, z the displacement, A the area of the plate, and ϵ the permittivity between plates. As the drive voltage reaches a threshold called the pull-in voltage, the displacement remains unchanged. If the movable electrode is attached to a spring, the pull-in occurs when the restoring force balances the electrostatic force,

$$V^2 = \frac{2Kz(g - z)^2}{\epsilon A} \tag{1.10}$$

The derivative of voltage to displacement is zero now, which leads to the deflation at the pull-in voltage,

$$\frac{d}{dz}(z(g - z)^2) = (g - z)(g - 3z) = 0 \tag{1.11}$$

$$Z_{PI} = \frac{g}{3} \quad (1.12)$$

Note that this deflation only depends on the gap. Substituting it into Equation 1.10 gives the pull-in voltage

$$V_{PI} = \sqrt{\frac{8}{27} \frac{Kg^3}{\epsilon A}} \quad (1.13)$$

Another type of electrostatic actuator is interdigitated combs. There are currently four categories of comb drive designs: lateral combs [17,18], rotary combs [19–21], staggered vertical combs (SVC) [22–27], and angular vertical combs (AVC) [28–33]. In the lateral combs, Figure 1.12a, the forces along the y direction are balanced and the combs move in the x direction. In an SVC actuator as shown in Figure 1.12c, a vertical offset between the moving combs and the fixed combs for out-of-plane rotation is required. In order to create the vertical offset between the two sets of combs, various fabrication techniques such as wafer bonding [22,25,27], integration of polysilicon and surface micromachining [23], and double-side alignment lithography on an SOI wafer [24,26] have been used. In the case of AVC illustrated in Figure 1.12d, the movable combs are often fabricated in the same layer as the fixed fingers and then tilted upward by various post-fabrication methods such as plastic deformation [30,31], residual stress [28], reflow of PR [29], and manual assembly [32,33]. In the lateral and vertical comb actuation setups, the force is independent of the displacement, unlike that of the parallel plate actuator setup. In addition, the force is inversely proportional to the gap distance making the force generated much smaller than that of the parallel plate actuator. This can be compensated by adding more fingers and applying a higher voltage.

In general, parallel plate and comb actuators are the available designs that may be used in bulk micromachined optical MEMS devices, while polysilicon-based comb actuators are often used in surface micromachined structures. Briefly speaking, parallel plate actuation can provide a large force ($\sim 50 \mu\text{N}$) with a small displacement ($\sim 5 \mu\text{m}$), but the force is highly nonlinear and unstable within the displacement range. On the other hand, interdigitated comb actuation provides a moderate level of force ($\sim 10 \mu\text{N}$) with a reasonable displacement ($\sim 30 \mu\text{m}$). Compared with other forms of actuation mechanisms, electrostatic actuation offers a fast response time ($\sim 1 \text{ms}$) with negligible power consumption and can be easily integrated with an electronic control. However, it faces many challenging issues such as low mechanical stability due to pull-in, non-linearity, and a very high actuation voltage ($\sim 50 \text{V}$).

1.2.3 Piezoelectric actuation

The piezoelectric effect is understood as the linear electromechanical interaction between the mechanical and the electrical states in a crystalline material. An applied DC voltage across the electrodes of a piezoelectric material will result in a net strain that is proportional to the magnitude of the electric field. A lack of a center of symmetry in a piezoelectric crystal means that a net movement of positive and negative ions with respect to each other as a result of stress will produce an electric dipole as shown in Figure 1.13. Adding up these individual dipoles over the entire crystal gives a net polarization and an effective field within the material. Conversely, a mechanical deformation of the crystal is produced when an electric field is applied, which makes this phenomenon extremely useful in driving optical MEMS devices [34,35].

In general, the piezoelectric effect is often described in terms of a piezoelectric charge coefficient, d_{ij} , which relates the static voltage or electric field in the i direction to the displacement of the applied force in the j direction. When a piezoelectric material is deposited on top of a microstructure, for example, an Si cantilever, axes 1 and 3 are defined as the longitudinal and normal

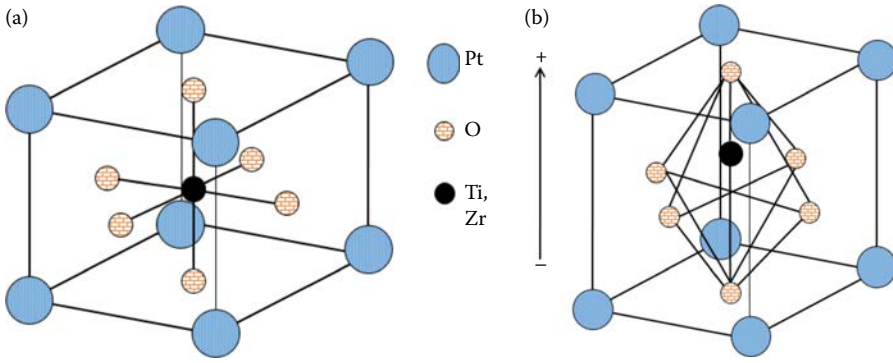


Figure 1.13 Schematic diagram illustrating the change in perovskite crystal structure (a) before and (b) after voltage is applied across it.

directions of the cantilever, respectively. The piezoelectric charge coefficients are given as d_{33} when both the voltage and force are along the vertical axis (axis 3), while d_{31} is used when the voltage is along the vertical axis, but the force generated is along the longitudinal axis (axis 1). The piezoelectric charge coefficient, which is the proportionality constant between strain and electric field, indicates that a higher value would be highly desirable for actuation purposes.

Considering a layer piezoelectric with two electrodes on both sides, the bending radius is

$$\frac{1}{R} = \frac{2d_{31}E_3(t_p + t_e)A_pE_pA_eE_e}{4(E_pI_p + E_eI_e)(A_pE_p + A_eE_e) + (A_pE_pA_eE_e)(t_p + t_e)^2} \quad (1.14)$$

Similar to a bimorph electrothermal actuator, the vertical displacement is

$$\delta = \frac{L^2d_{31}\frac{V}{t_p}A_eE_eA_pE_p(t_p + t_e)}{4(A_eE_e + A_pE_p)(E_pI_p + E_eI_e) + (t_e + t_p)^2A_eE_eA_pE_p} \quad (1.15)$$

where t_p , t_e , A_p , A_e , E_p , E_e , I_p , and I_e are the thicknesses, cross-section areas, Young's moduli, and moments of the piezoelectric (p) and elastic (e) layers. L is the length of the layer.

Most of the piezoelectric materials have a perovskite crystal structure and they include quartz (SiO_2), lithium niobate (LiNbO_3), aluminum nitride (AlN), zinc oxide (ZnO), and lead zirconate titanate (PZT), while the most well-known polymer-based piezoelectric material is polyvinylidene fluoride (PVDF). Among these materials, PZT has the largest piezoelectric charge coefficients (d_{31} and d_{33}) as shown in Table 1.1 [36]. Due to its excellent piezoelectric properties, PZT has often been used in numerous optical MEMS applications such as adaptive optics [37,38], optical

Table 1.1 Piezoelectric coefficient of selected piezoelectric materials

Material	Piezoelectric coefficients
Barium titanate	$d_{33} = 85.6 \text{ pm/V}$; $d_{31} = 34.5 \text{ pm/V}$
Aluminum nitride	$d_{33} = 4.5 \text{ pm/V}$
Zinc oxide	$d_{33} = 12.4 \text{ pm/V}$
Lead zirconate titanate	$d_{33} = 360 \text{ pm/V}$; $d_{31} = 180 \text{ pm/V}$
Polyvinylidene fluoride	$d_{33} = 20 \text{ pm/V}$; $d_{31} = 30 \text{ pm/V}$

Source: Adapted from Y. Eun et al. *Sensors and Actuators A: Physical*, vol. 165, pp. 94–100, 2011.

communication [39,40], and beam scanning [41–43]. However, unlike AlN, PZT is not CMOS compatible, hence making mass production by CMOS foundries impossible.

1.2.4 Electromagnetic actuation

Lorentz force is generated when a current-carrying element is placed within a magnetic field and it occurs in a direction equivalent to the cross product of the current and magnetic field. A simple example is the rotation of a soft magnetic cantilever, whose thickness t and width w are much shorter than its length L . If it is placed in a uniform magnetic H_0 field, the magnetic torque on the beam is [44,45]

$$\tau_{\text{magnetic}} = m \times B_0 = \mu m \times H_0 \quad (1.16)$$

where B_0 is the magnetic induction and m the magnetic moment, defined as

$$B_0 = \mu H_0 m = MV \quad (1.17)$$

where μ is the permeability constant, M the magnetization in the beam, and V the volume. When the magnetic force is large enough to deform the beam, the relationship between the corresponding torque and displacement $\Delta\delta$ at the free end is

$$\tau_{\text{magnetic}} = \frac{3EI\Delta\delta}{L^2} = \frac{Ewt^3\Delta\delta}{4L^2} \quad (1.18)$$

E is Young's modulus of the beam and I the moment of inertia. To enlarge the deformation, a larger magnetic field can be applied, thus producing stronger magnetization in the cantilever.

Although Lorentz force actuation may be applied to MEMS devices in a number of ways, the prevailing approach is to have metal coils integrated on a micromirror and actuated by an AC current at resonance when the mirror is placed near a permanent magnet [46–52]. Asada et al. proposed the two-dimensional scanner using electromagnetic coupling between a driving coil and a detection coil [46]. Figure 1.14a shows a three-axis actuated micromirror developed by Cho et al., where actuation coils made of gold are electroplated on the mirror plate and cantilever actuators

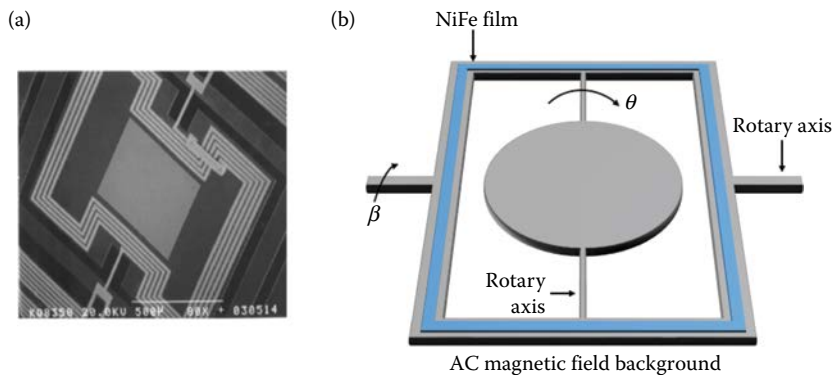


Figure 1.14 (a) A SEM photo showing the electroplated gold electromagnetic coils on the mirror plate and actuated by AC current at resonance in the presence of permanent magnet. (b) A schematic diagram illustrating a permanent magnetic film integrated on the mirror plate and actuated by the surrounding AC magnetic field. (From I.-J. Cho and E. Yoon. *Journal of Micromechanics and Microengineering*, vol. 19, p. 085007, 2009.)

[52]. Another approach, as shown in Fig. 1.14b, is to integrate a permanent magnet (hard ferromagnet) or a permalloy layer (soft ferromagnet) on a movable mirror while a Lorentz force is introduced through the interaction between the magnetic layer and surrounding AC magnetic field of an external solenoid [53–57]. The availability of permanent magnetic materials that are compatible with MEMS processing is limited and this produces a difficulty in the necessary process development. Thus, it is common for the magnetic field to be generated externally, while the discrete and movable electromagnetic actuators often comprise metal coils.

Similar to electrostatic actuation, electromagnetic actuation provides moderate switching speed (~ 10 ms) and low power consumption (~ 100 mW), but the assembly of permanent external magnets and coils make it extremely challenging. Fabricating ferroelectric materials can also be challenging, as these thin films may not be compatible with the standard CMOS processes.

1.3 Optical MEMS for imaging

We now discuss the applications of MEMS-driven mirrors in imaging systems. Such systems usually use single-pixel-based photodetectors (can be a single fiber coupled to a detector) and employ MEMS mirrors to rapidly steer their instantaneous field of view (IFOV) from point to point in a sequential way across the system field of view (FOV) to achieve image acquisition. There are several advantages for such systems. For example, using MEMS mirrors and single-pixel detectors, the imaging system can be constructed in a very compact package. This is attractive to biomedical imaging applications where the sizes of the imagers are often critical. In addition, it is easier for such systems to incorporate different types of imaging modalities, for instance, realization of 3D imaging deep into biological samples through laser confocal scanning [58] and the optical coherence tomography (OCT) approach [59].

Taking the scanning confocal imaging shown in Figure 1.15a as an example, a point light source (usually from a laser) is collimated with lens 1, reflected by a beamsplitter, and focused into the sample with lens 2. The scattered or emitted light by the sample is then collimated again with lens 2, passed through the beamsplitter, and focused by lens 3 to a confocal plane. A small pinhole is

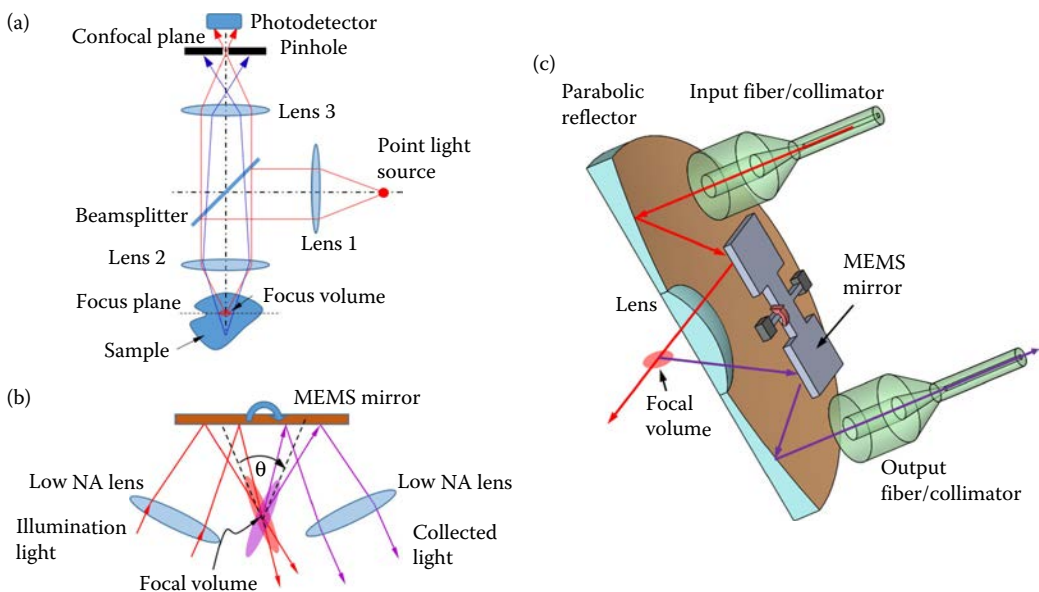


Figure 1.15 Schematic illustrations of (a) a scanning confocal microscope, (b) a dual-axis scanning configuration, and (c) a miniature dual-axis scanning confocal microscope.

then placed at the confocal plane, which forms a conjugated pair with the focus spot in the sample. Light passing through the pinhole is then received by a photodetector. In this configuration, only light scattered/emitted within a tiny volume (focus volume) inside the sample can pass through the pinhole and be detected, while light from outside the focus volume (above or below the focus plane) is blocked by the pinhole. To achieve imaging, an optical scanner (not shown in the figure for simplicity) is usually employed, which deflects the light beam and scans the focus spot across the two dimensions in the focus plane. In this way, a 2D image of the sample slicing at the focus plane is obtained. Light from the layers above or below the focus plane is rejected by the confocal pinhole mechanism. A 3D image of the sample can then be obtained through a layer-by-layer image acquisition by further moving the sample toward and/or away from the imaging optics. Benchtop confocal imaging microscopes are now widely available in the market.

With MEMS technology, a number of miniature confocal microscopes are reported [60–63]. They feature significantly reduced package sizes and can be handheld for clinical applications such as *in vivo* skin imaging [64]. Some of them are constructed with diameters small enough to be put into endoscopic platforms [65,66]. In such MEMS confocal microscopes, the beamsplitter in Figure 1.15a is replaced with a MEMS scanning mirror and an optical fiber is usually used as the point light source. The light is scanned by the MEMS mirror and focused onto the sample. The scattered or emitted light from the focus volume is collimated, de-scanned by the same MEMS mirror, and focused into the same input fiber. In this case, the fiber acts as both the point light source (due to its small core diameter) and the pinhole. This configuration is widely used and is also applicable to nonlinear optical microscopy such as coherent anti-Stokes Raman scattering (CARS) imaging [67], Raman spectroscopy [68], and two-photon imaging [69,70].

Recent developments in this field have also extended the design to a dual-axis scanning configuration [28,71–73], as shown in Figure 1.15b. It is well known there are certain limitations for the confocal imaging systems shown in Figure 1.15a. For example, lenses with large numerical apertures (NA) are needed for high resolution (especially for high axial resolution) imaging, which unfortunately leads to short working distances, low penetration depths, and reduced contrast. Dual-axis confocal imaging as shown in Figure 1.15b elegantly solves these problems by constructing the light illumination and collection in two different paths [30,74]. In this way, low NA lenses can be used leading to increased working distances. In addition, since the collection optics is tilted to an angle θ with respect to the illumination optics, the small focus volume is still obtained by the intersection of the illumination and collection paths despite the long depth of focus of the low NA lenses. This configuration also significantly rejects light from the illumination path outside of the focus volume thus leading to enhanced contrast. A schematic showing the construction of the dual-axis MEMS confocal microscope using two fibers, a parabolic reflector, a lens, and a MEMS-driven scanning mirror is illustrated in Figure 1.15c.

An endoscopic OCT system is another example of successful applications based on optical MEMS imaging technology. A standard OCT setup using a fiber-based Michelson interferometer is illustrated in Figure 1.16a [75]. The setup utilizes low coherence light to capture 3D images of biological tissues or samples, which are typically high scattering media. Compared with confocal imaging, OCT imaging usually results in a larger penetration depth into the tissue with a slightly lower resolution. OCT systems use low coherence or broadband light sources with typical coherent lengths of only a few micrometers. Light is then simultaneously sent into the reference and measurement arms with a fiber coupler (or a beamsplitter for a free-space Michelson interferometer). Light reflected from the reference and measurement arms is then recombined to form interference. It is well known that the interference pattern can only be formed if the optical path difference (OPD) between the reference and measurement paths is smaller than the coherent length of the light source, which is only a few microns for OCT systems. This defines the depth resolution and creates a “coherent gate” effect that isolates the light signals scattered within a thin slice at a specific depth under that sample surface and rejects other light signals from other locations. The 2D image of the slice is obtained again through point-by-point scanning using a mirror, and the full 3D image of the sample is obtained by an additional depth scanning by moving the reference

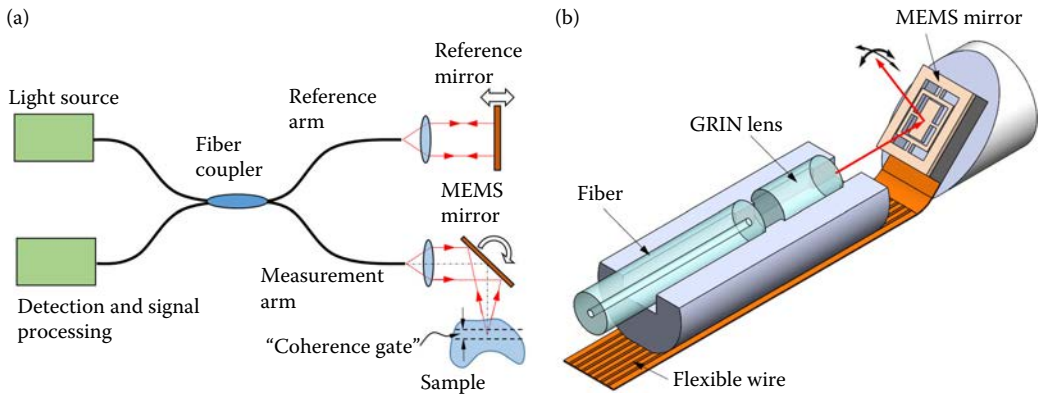


Figure 1.16 (a) Optical coherence tomography (OCT) in a basic configuration, and (b) a side-view MEMS-based endoscopic OCT probe.

mirror as shown in the figure. In addition to this standard configuration, there are many other OCT configurations such as Fourier domain OCT and swept-source OCT [76].

As shown in Figure 1.16a, MEMS-driven mirrors are usually employed in OCT systems to act as scanning mirrors in the measurement arm to rapidly steer the field of view. The application of optical MEMS scanning results in compact systems such as handheld OCT systems for *in vivo* tissue imaging (skin and eye imaging, for example) [77] and endoscopic OCT probes for imaging of internal organs [78]. A typical design of a side-view MEMS OCT probe is shown schematically in Figure 1.16b. Light is launched into the probe using an optical fiber. It is then focused by a gradient index (GRIN) rod lens, reflected by a MEMS mirror, and continues to focus into the tissue/sample under examination. The light reflected from the tissue/sample is de-scanned by the same mirror, collected by the same GRIN lens and fiber, and sent into the fiber Michelson interferometer for signal processing. Apart from side-view probes, full 360° circumferential scanning probes [79,80] and forward-view MEMS OCT probes are also demonstrated [81]. The use of MEMS scanning mirrors here is very attractive due to the following reasons. First, the ultra-small footprints of MEMS mirrors facilitate the miniaturization of OCT probes, which is critical for endoscopy applications. Second, the low inertia and fast scanning characteristics of these mirrors also enhance the image acquisition rate making real-time OCT imaging possible. Third, MEMS mirrors are low cost due to IC-like fabrication processes thus making such MEMS endoscopic OCT probes affordable. A wide variety of MEMS mirrors for OCT imaging have been reported, including those driven by electrostatic [82,83], electromagnetic [84], piezoelectric [85], and electrothermal actuators [86–88]. Each of those driving mechanisms has their own advantages and disadvantages. Overall, however, the electrothermal MEMS mirrors seem to be more suitable for MEMS endoscopic OCT probes due to their very low driving voltage (important for safe operation inside the human body) and large optical scan angle despite their relatively slow response time.

1.4 Optical MEMS for displays

Optical MEMS also plays an important role in the display industry [89]. Display devices can be categorized as projection displays, transmissive displays, and reflective displays according to their operation modes. Optical MEMS technology has been successfully applied to all of these displays. In addition, based on their working principles, optical MEMS displays can be divided into scanning-based and non-scanning-based displays. The former can be further divided into point source 2D scanning and linear array 1D scanning-based displays. In this section, we will briefly discuss some of the most successful devices and systems.

1.4.1 Scanning-based MEMS displays: Point source 2D scanning

There are generally two configurations for MEMS displays using the point source 2D scanning approach, with one having two MEMS mirrors each scanning a single direction and the other having a single MEMS mirror scanning in both directions. This type of scanning projection display has very small form factors and thus can be incorporated into wearable and mobile projection systems [90]. The performances of these 2D scanning-based displays, including frame rate, resolution, and brightness, are generally determined by those of the optical MEMS scanners and lasers employed.

As shown in Figure 1.17a, using two 1D optical scanners with one scanning the incident optical beam in the horizontal direction at a faster rate and the other scanning the beam in the vertical direction at a slower rate, one can project a raster scan pattern on a project screen. By modulating the light intensity according to its position on the screen, images and videos can be displayed. Three lasers (red, green, and blue) can be used and projected simultaneously with the same mirrors for color displays. This configuration is among the early types of the point source 2D scanning MEMS displays demonstrated [91]. The light beam wandering on the second mirror and the raster scan pattern distortion caused by the inherent spatial separation between the two scanning mirrors are usually among the major limitations of this kind of configuration.

A more compact solution has been developed that uses a single MEMS mirror scanning in both directions as shown in Figure 1.17b. Examples include the mobile projection systems developed by Microvision Inc. [46] and Fraunhofer Institute of Photonic Microsystems [92]. These MEMS mirrors typically have gimbaled suspensions that allow them to simultaneously rotate about a fast axis and a slow axis. The MEMS driving mechanisms include electrostatic [93], electromagnetic [49], and piezoelectric [94] actuations. An example of electromagnetic actuation is illustrated schematically in Figure 1.17b. As shown, an electric coil is integrated in a movable frame of the scanner and the driving current is modulated. The scanner is placed in a magnetic field produced by an external permanent magnet. The modulated current generates oscillating torques that drive the movable frame (together with the mirror) into a slower sawtooth scanning and the inner mirror into a faster oscillation about its axis at its resonant frequency.

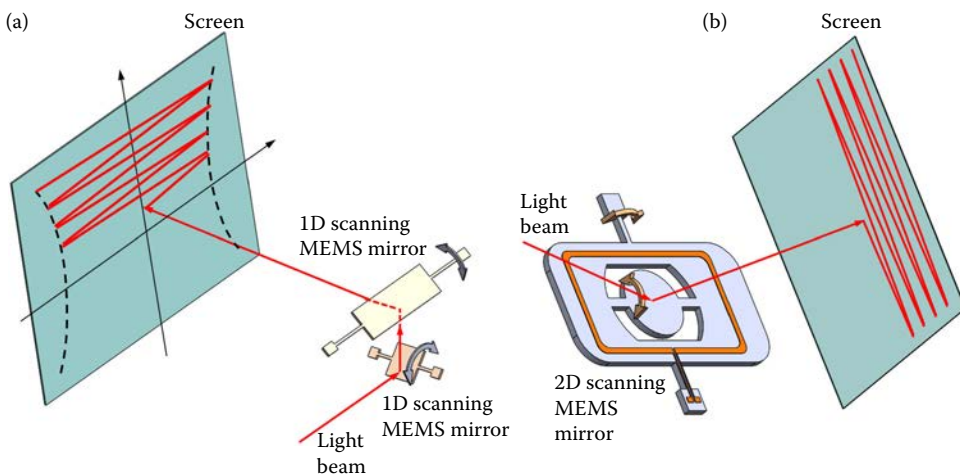


Figure 1.17 Schematics of the point source 2D scanning displays, (a) with two 1D scanning MEMS mirrors, and (b) with a single MEMS dual-axis mirror scanning in two directions.

1.4.2 Scanning-based MEMS displays: Linear array 1D scanning

In point source 2D scanning MEMS displays, one direction is usually scanned at a very fast rate (about tens of kHz) to meet the frame rate requirement of the display. This creates significant acceleration and deceleration forces on the MEMS mirror plate, thus the mirror is subjected to dynamic deformation which can potentially blur the light spot size and reduce the display resolution. Hence, considerations have to be taken in the mirror design to keep this dynamic deformation small enough (i.e., smaller than $\lambda/8$) to meet the Rayleigh wavefront criterion for a good imaging system. On the other hand, one can also construct a display system using a linear array of light sources, instead of a point light source, to display a line image on the screen and then scan this line in its perpendicular direction across the screen. This configuration only requires a slow 1D scanning mirror.

A typical linear array device is the grating light valve (GLV) [95]. Figure 1.18a shows one of its pixels, which usually consists of six micron-sized coated high reflectivity ribbons. At the initial state, all ribbons are in the same plane and the pixel essentially behaves like a mirror that reflects the incident light back creating a “dark” state. On the other hand, when the alternating ribbons are actuated, pulling down toward the substrate with a precise displacement of a quarter wavelength ($\lambda/4$), the pixel then behaves like a diffraction grating. Furthermore, the lights reflecting off the top and bottom ribbons are in destructive interference, thus distributing almost all light energy into the \pm first diffraction order and creating a “bright” state for the pixel. This state switching is very fast and can happen at the order of tens of nanoseconds owing to the extremely small inertia of the ribbons. Since the GLV can only have “dark” and “bright” states, a pulse width modulation (PWM) scheme [96] is used to generate grayscale images with various levels of light intensity at each pixel. In other words, when a GLV pixel is switched to the “bright” state longer in a video frame time, it appears brighter. Figure 1.18b then shows schematically how the pixels are arrayed into a linear array, and a projection system employing a GLV device is illustrated in Figure 1.18c. Since GLV utilizes the first diffraction order as the light source for projection, its zeroth diffraction order has to be blocked. Usually, this can be achieved through employment of a 4-f optical filtering system in the projection optics as shown in Figure 1.18d [97].

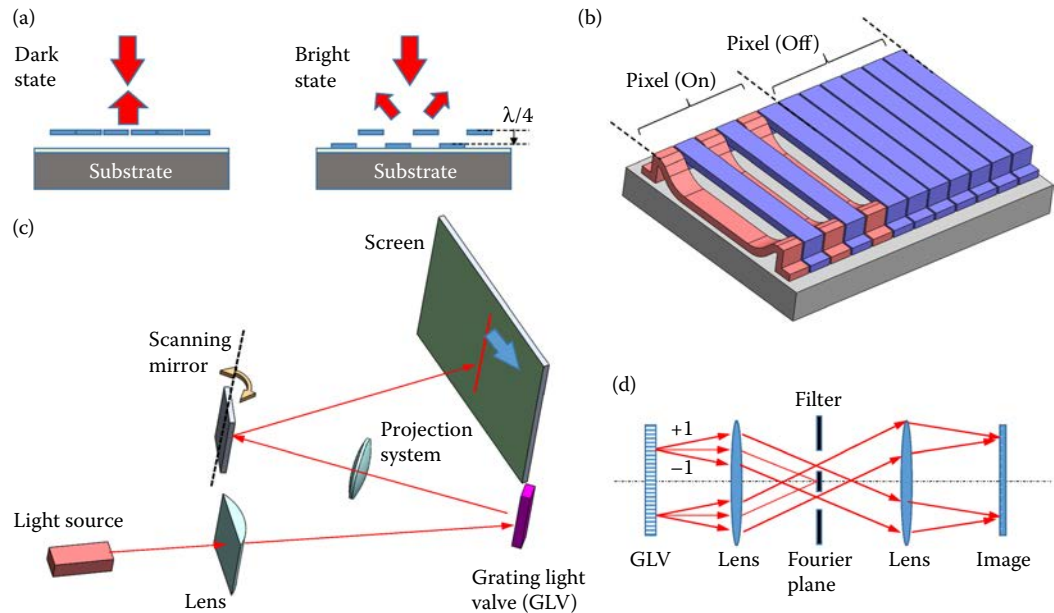


Figure 1.18 (a) Operation principle of the grating light valve (GLV), (b) schematic showing two GLV pixels, (c) schematic of the linear array 1D scanning display using GLV, and (d) optical filtering system for the GLV-based projection display.

1.4.3 Non-scanning-based MEMS displays

Non-scanning-based MEMS displays do not have any light scanning mechanisms and usually have a 2D array of pixels. The most well-known example of this kind of MEMS display is the digital light processing (DLP™) projection displays from Texas Instruments (TI) [98]. At the core of this projection display is the digital micromirror device (DMD), which contains a large number of bistable micromirrors (can be over a million depending on the display format). As shown in Figure 1.19a, each square micromirror has a width of about 15 μm and represents one pixel. It can be driven by its integrated COMS circuitry to rotate $+10$ degrees about an axis defined by a pair of torsional springs hidden underneath the mirror representing a “bright” or “ON” state or -10 degrees representing a “dark” or “OFF” state. The switching time is very fast at the microsecond level due to the low mirror inertia. Grayscale images are again achieved through a PWM scheme by controlling each mirror’s “ON” state time during each frame. A schematic showing the use of a DMD in a projection display system is illustrated in Figure 1.19b. Absorbers can be used to absorb the light reflected from those micromirrors in the “dark” state. To display color images or videos, two approaches can be used [99]. One uses a rotating color wheel filter to separate each video frame into its constituent R, G, and B fields, and sequentially illuminate a single DMD with the R, G, and B light beams. The viewer’s eye integrates sequential images to obtain a full color image. The other approach uses three DMDs instead of one. White light is first divided into RGB light beams using filters, which are then directed to their own DMD chips. Upon reflection from those chips, they are recombined and projected onto the screen. TI’s DLP technology is currently applied to a wide range of applications including TVs, cinema projection systems, and mobile projectors.

Digital micro-shutters (DMS) developed by Pixtronix is another MEMS-based display technology in this category [100]. As shown in Figure 1.20a, DMS technology is built upon standard thin film transistor (TFT) liquid crystal display (LCD) manufacturing technology and incorporates MEMS. As shown in the figure, the working principle of a DMS device mainly consists of the following key features; an optical architecture with a light-recycling LED backlight, an optical aperture layer, and a MEMS layer containing an array of micro-shutters. The MEMS micro-shutter is actuated by the electrostatic force and can move laterally to open or block the aperture, thus creating “bright” and “dark” states for each pixel. Field sequential color with high color changing

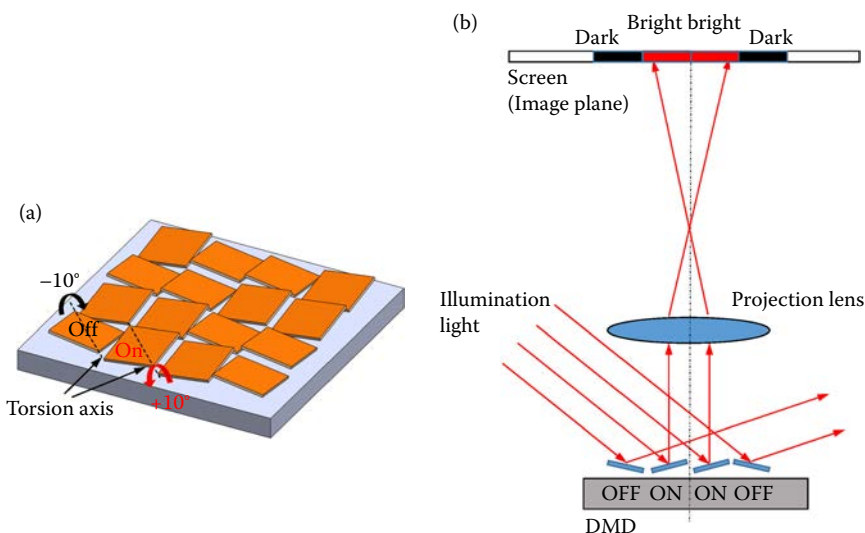


Figure 1.19 (a) Schematic of a DMD chip and (b) schematic of a projection display using TI’s DMD.

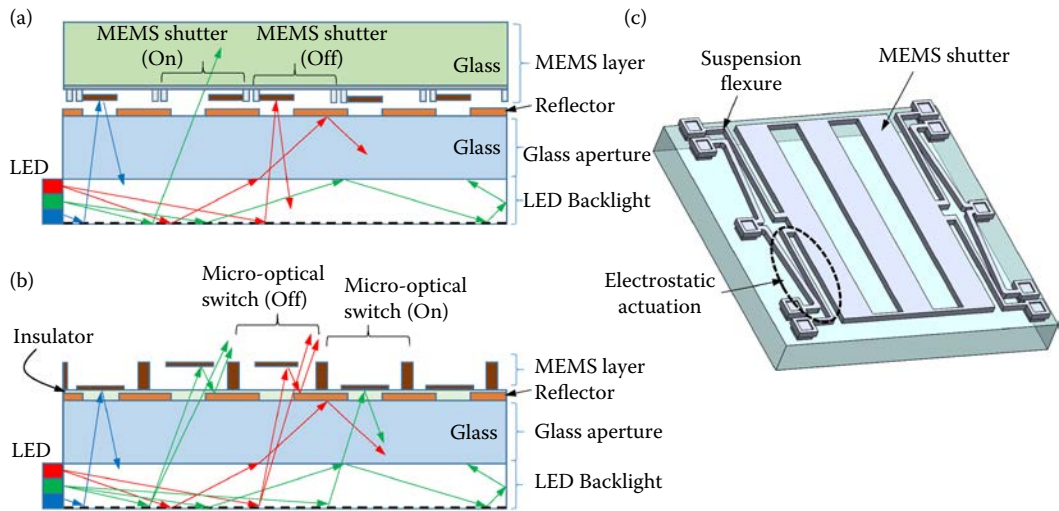


Figure 1.20 Schematics of (a) a transmissive display using digital micro-shutters (DMS), (b) a transmissive display using micro-optical switches, and (c) an electrostatically-driven MEMS micro-shutter.

frequencies is employ to create color images, thus no additional optical filters and polarizers are needed as compared with traditional LCD displays. The use of reflective surfaces of the apertures and micro-shutters to recycle the light energy also makes the display devices energy efficient. A typical MEMS micro-shutter design using four suspension flexures is illustrated in [Figure 1.20c](#). Another similar concept of such a MEMS displays is also proposed, a schematic of which is illustrated in [Figure 1.20b](#) [101]. As shown, instead of using lateral MEMS shutters, the “bright” and “dark” states of the pixels are created by moving micromirrors up or down perpendicular to the aperture surface for opening or closing apertures. In the “bright” state, the light is coming out of the pixel through multiple reflections or direct leakage.

As discussed above, TI’s DLP™ is mainly used for projection displays, while Pixtronix’s DMS is mainly used for transmissive displays. There is yet another MEMS non-scanning display technology termed a interferometric modulator display (IMOD) developed by Qualcomm, which is mainly used for reflective displays [102,103]. IMOD operates and generates colors using the light interference effect, that is, in the same way as butterfly wings and bird feathers create colors using microscopically structured surfaces. As shown in [Figure 1.21a](#), each pixel of the IMOD display is similar to a Fabry–Pérot interferometer, which consists of a thin film stack and a reflective mirror separated by an air gap. The light reflected off of the thin film and the mirror interfere constructively at certain wavelengths and destructively at others, thereby producing a colored effect on the pixel. If the air gap is reduced, the constructive wavelength blue-shifts thus changing the pixel color. The early versions of the IMOD displays are operated in digital mode, where each pixel is further divided into R, G, and B subpixels, each with a designated air gap, as shown in [Figure 1.21b](#). If a driving voltage is applied across the flexible membrane-like mirror and the film stack, the electrostatic force drives the mirror to move up toward the thin film stack causing the air gap to collapse. This shifts the constructive interference wavelength to ultra-violet (UV) wavelengths, and the subpixel will display a “dark” state. When the voltage is released, the mirror returns to its original position, and the subpixel returns to its designated color. The switching time between the “color” and “dark” states is fast, in the range of 10 microseconds. A new generation of IMOD displays has also been developed by Qualcomm that uses a single pixel to produce multiple colors [104]. Each pixel is identical, and through precisely controlling the air gap, it can continuously tune its reflective color across the visible spectrum. An IMOD display can be viewed using only ambient light and thus has low power consumption and is energy efficient.

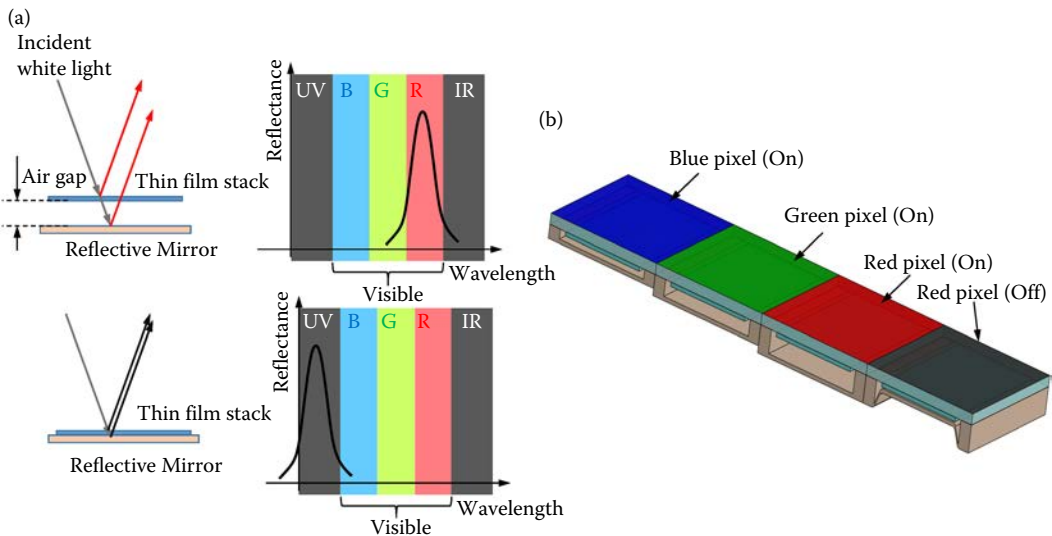


Figure 1.21 (a) Operation principle of the interferometric modulator display (IMOD) and (b) a schematic showing the structures of the red, green, and blue subpixels.

1.5 Optical MEMS for sensing

Optical MEMS technology is also extensively used in sensors. Based on their sensing mechanisms, these devices can be categorized into two groups, coherent and noncoherent optical sensors. Coherent-based sensors rely on various light interference effects for sensing, hence coherent light sources such as lasers are typically used. On the other hand, noncoherent-based sensors do not depend on light interference, and they typically detect variations of light intensities as functions of measurands.

1.5.1 Noncoherent optical MEMS sensors

Figure 1.22 shows typical examples of noncoherent optical MEMS sensors. One sensing principle is based on the well-known “light lever” effect, in which a measurand changes the orientation of a mirror thereby altering the direction of a light beam reflected off of it. The change of the beam direction is then converted into beam spot movement on a position-sensitive photodetector (PSD). A four-quadrant photodiode, which consists of four identical light-sensitive surfaces separated by small gaps, is usually employed for this type of position sensing. The system is initially set up so that the light energy is equally distributed to the four quadrants and the outputs of the diodes are equal. When the beam spot moves, the diode outputs change. In this case, the difference between the left and right quadrants indicates horizontal movement and the difference between top and bottom quadrants indicates vertical movement. This sensing configuration can be very sensitive owing to the fact that the movement of the light spot is significantly amplified if the mirror-to-detector distance is large. A large number of sensors are demonstrated with MEMS fabricated cantilevers using this sensing mechanism, as shown in Figure 1.22a. These include atomic force microscopes (AFM) and chemical/biological sensors including those used for the detection of antigen and antibody bonding events [105]. While out-of-plane motion can easily cause light beam deviation with the help of a cantilever or a mirror, in-plane motion is slightly more complicated and such a light beam deviation scheme can be achieved with the help of a diffraction grating as shown in Figure 1.22b. The in-plane rotation of the grating changes the orientation of the grating lines thereby inducing a change of direction for a selected non-zeroth-order diffracted beam. Such a grating-based sensing

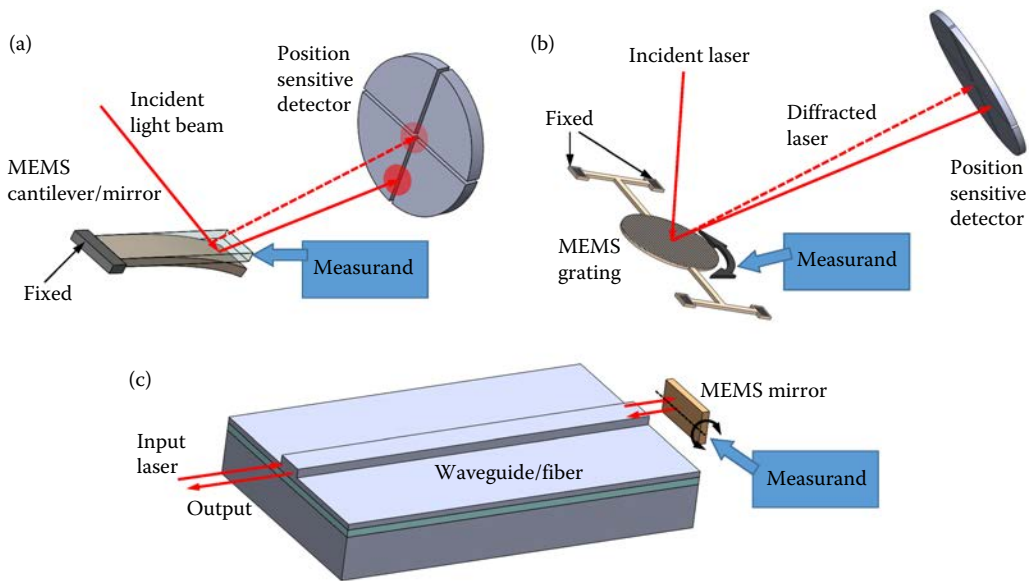


Figure 1.22 Schematics of the noncoherent optical MEMS sensors. (a) Sensing mechanism using “light lever” effect with a cantilever, (b) sensing mechanism using “light lever” effect with a MEMS grating, and (c) sensing mechanism based on light coupling to waveguides/fibers.

mechanism has been utilized to demonstrate a sensitive integrated MEMS tribometer [106]. These optical MEMS sensors based on the “light lever” effect are very sensitive. However, they have large footprints because the mirror-to-detector distances required are usually large.

There is another type of noncoherent optical MEMS sensor that uses light waveguiding and a coupling effect as shown schematically in Figure 1.22c. As shown, light is launched into an input waveguide (or fiber) and directed toward a mirror. Upon reflection from the mirror, the light is coupled back into an output waveguide (or fiber). The output waveguide can be a new waveguide or the same waveguide as the input waveguide. In this configuration, it is well known that the light coupling efficiency is very sensitive to the motion of the mirror. Hence, translational motion (varying the gap spacing between the mirror and the waveguide) or rotation (tipping or tilting) of the mirror caused by the measurand can drastically change the light intensity in the output waveguide. Several sensors such as magnetic field sensors and accelerometers are reported based on such a sensing mechanism [107]. It is noted that this type of optical coupling-based sensors, unlike those based on the “light lever” effect, can be miniaturized and integrated at a chip scale.

1.5.2 Coherent optical MEMS sensors

A majority of optical MEMS sensors are coherent-based sensors utilizing lasers and various light interference effects. They are essentially miniaturized optical interferometers developed using MEMS technology. In the following sections, we mainly focus on those that incorporate MEMS mirrors. For each interferometer type, we discuss two types of construction approaches, namely the out-of-plane (utilizing mirror surfaces parallel to the substrate) and in-plane (utilizing mirror surfaces perpendicular to the substrate) construction approaches. For the latter, silicon-on-insulator (SOI) wafers are typically used and mirrors are formed using deep-etched side walls. It should be noted that there are many other types of optical MEMS coherent-based sensors built on waveguide technology, such as a chemical/biological sensor using an integrated Mach–Zender interferometer as shown in Figure 1.23 [108]. The change of the refractive index in the measurement arm in close proximity to the waveguide surface varies the effective optical path length due

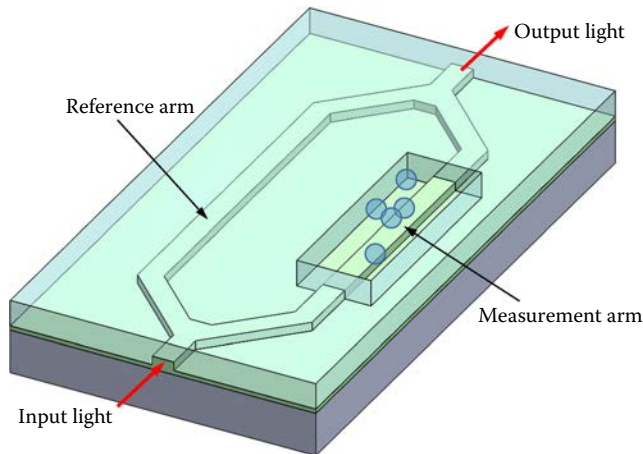


Figure 1.23 A waveguide-based Mach–Zehnder interferometer for biochemical sensing.

to the presence of a given chemical/biological analyte, thus changing the light interference and the interferometer's output.

1.5.2.1 Optical MEMS sensors based on Michelson interferometers

The Michelson interferometer is perhaps one of the most commonly used interferometers in optics. As shown in [Figure 1.24a](#), the amplitude of the collimated incident light radiation is equally divided in a beamsplitter into two waves. They are reflected by two mirrors and recombined to form interference at the detection plane where photodetectors are located. For optical MEMS sensing applications, one mirror is usually fixed and the other is a movable MEMS mirror. The intensity of the interference signal detected varies as a function of the optical path difference (OPD) δ between the reference and measurement arms. The relationship is as follows:

$$I(\delta) = 0.5I_{\sigma}(1 + \cos 2\pi\sigma\delta), \quad (1.19)$$

where σ and I_{σ} are, respectively, the wavenumber ($\sigma = 1/\lambda$, λ being the wavelength) and intensity of the light source. Clearly, if a measurand (force, acceleration, etc.) causes the MEMS movable mirror

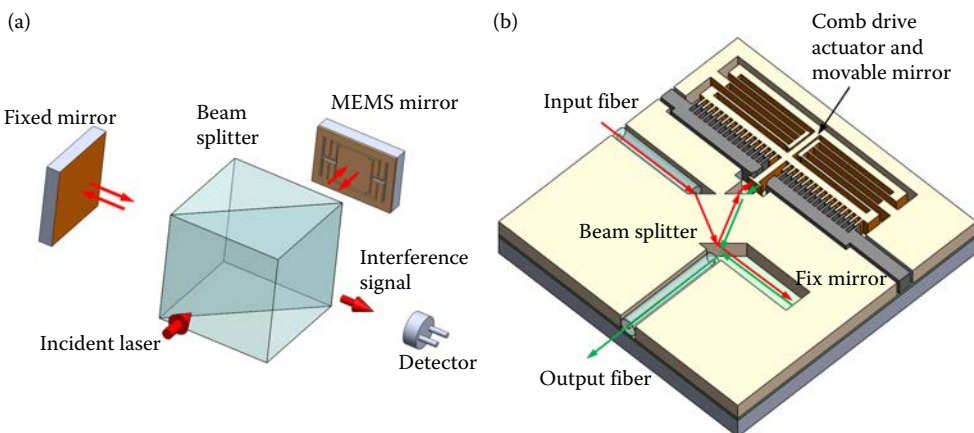


Figure 1.24 Optical MEMS-based Michelson interferometers in (a) out-of-plane construction and (b) in-plane construction using silicon-on-insulator (SOI) micromachining.

to move inducing a variation in the OPD δ , the output intensity from the interferometer varies, thus the measurand is detected. From the above equation, it is clear that the sensors built on such a light interference effect are inherently sensitive owing to the fact that the wavelengths of the light sources (lasers) used are usually at sub-micrometer levels.

Michelson interferometers are more frequently used for construction of Fourier transform infrared (FTIR) spectrometers, which are powerful tools for chemical analysis. In an FTIR system, the movable mirror is scanned over a range and the interferometer output light intensity variation $I(\delta)$ is recorded as a function of the OPD δ , which is usually called the interferogram. It can be shown that the light source power spectrum I_σ and the recorded interferogram are related by a Fourier transform [109]:

$$I_\sigma \propto \int_{-\infty}^{\infty} [I(\delta) - 0.5I(0)] \exp(-i2\pi\sigma\delta) d\delta, \quad (1.20)$$

where $I(0)$ is the intensity of the interferometer output at zero OPD. It can also be shown that the spectral resolution of the FTIR spectrometer is inversely proportional to the maximum OPD scan range provided by the movable mirror [109].

Conventional FTIR spectrometers are bulky, expensive, and limited to lab use. In recent years, the market has seen a high demand for low-cost miniaturized field-applicable FTIR spectrometers with relatively lower resolution, but capable of delivering cost effective real-time information for sensing applications in a wide variety of disciplines and industries, including environmental monitoring and food/beverage safety screening. In response to this, a number of miniaturized versions of FTIR spectrometers implemented with optical MEMS technology have been reported [110]. Similar to other optical MEMS interferometers, these miniature FTIRs are constructed in two ways. As shown in Figure 1.24a, for out-of-plane construction, the beam splitter, fixed mirror, and the MEMS movable mirror are separate components. They are aligned and assembled to form a Michelson interferometer. The MEMS mirror is typically operated in an out-of-plane mode moving translationally perpendicular to the device surface. A large stable travel range is also required in order to obtain sufficient OPD scanning for a high enough spectral resolution. The reported MEMS mirrors for FTIR spectrometers are typically driven by electrostatic, electrothermal [111,112], and electromagnetic actuation methods. Millimeter scale travel ranges have been demonstrated for some of those MEMS mirrors. Although this type of MEMS FTIR spectrometer has a relatively large footprint, they can potentially achieve good performances due to their high-quality mirror surfaces and large OPD scan ranges.

Another way of constructing optical MEMS miniature FTIR spectrometers is to build Michelson interferometers in a silicon device layer on an SOI wafer [110,113,114]. As shown in Figure 1.24b, the input and output fibers are, respectively, used to guide the light to the interferometer and collect the interference signal and guide it to the detector. Light propagates in the silicon device layer beneath the layer surface; hence this layer has to be thick enough, which is usually about a hundred micrometers. Deep reactive ion-etched silicon side-wall surfaces are utilized as the mirrors and beam splitters. Thermal oxidation and HF treatment can be used to reduce the side-wall surface roughness and improve the optical quality. Coatings can also be used to enhance the mirror's reflectivity. These types of optical MEMS FTIR spectrometers have compact sizes, but their spectral resolutions are usually limited.

1.5.2.2 Optical MEMS sensors based on lamellar grating interferometers

As shown in Figure 1.25a, a lamellar grating consists of an array of identical micromirrors, where alternating mirrors are grouped together. One group of the mirrors is usually fixed, while the other is movable. Driven by a measurand, the movable mirrors move with respect to the fixed mirrors, thus introducing an OPD between the light beams reflected off the surfaces of the two groups of

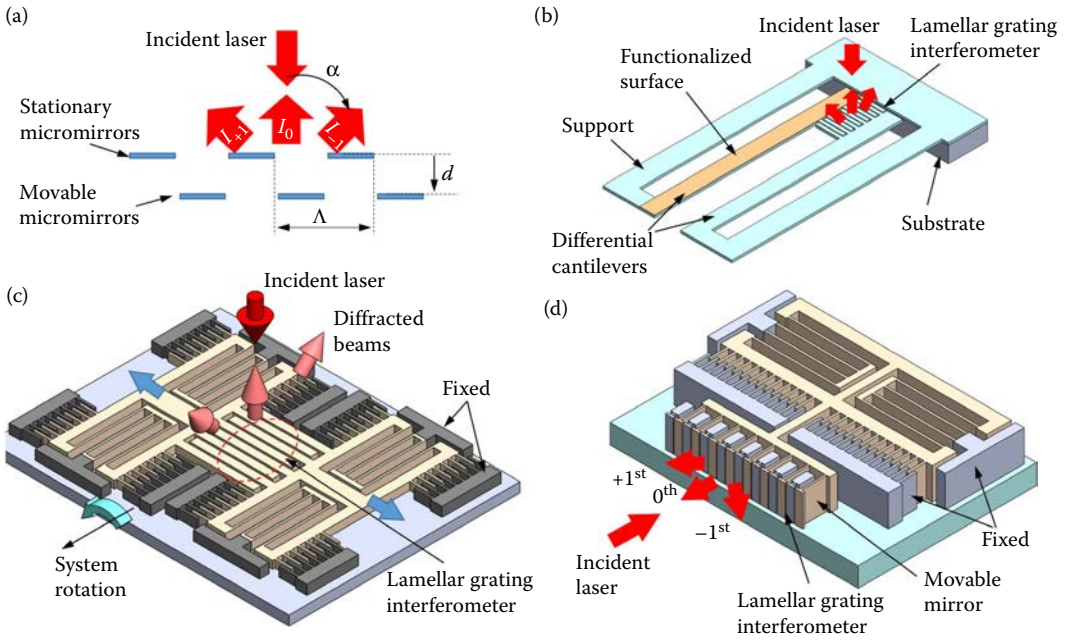


Figure 1.25 (a) Operation principle of the lamellar grating interferometer, (b) schematic illustration of a lamellar grating-based biochemical sensor, (c) a lamellar grating interferometer-based MEMS gyroscope, and (d) a lamellar grating-based FTIR spectrometer.

mirrors. The lamellar grating essentially behaves like a diffraction grating with varying grating groove depths. As a result, the intensities of the diffracted beams are dependent on the mirror separation gap d [115]. Assuming normal light incidence, the relationship is as follows:

$$I \propto \left(\frac{\sin K}{K} \right) \left(\frac{\sin 2NK}{2K} \right) (1 + \cos 2\pi\sigma\delta), \quad (1.21)$$

where $K = (\pi\sigma\Lambda)\sin(\alpha)/2$, σ is the incident wavenumber $\sigma = 1/\lambda$, λ is the wavelength, and Λ and N are the grating period and the number of periods illuminated, respectively. The diffraction angle α and the OPD δ are given as follows:

$$\sin\alpha = \frac{m\lambda}{\Lambda}, \quad (1.22)$$

$$\delta = d \left(1 + \cos\alpha + \frac{\Lambda}{2d} \sin\alpha \right), \quad (1.23)$$

where m is the diffraction order.

It is clear that all diffracted beam intensities vary as the OPD δ changes, hence any order can be used for sensing applications to detect the movement d . However, the zeroth-order is usually preferred. The lamellar grating interferometer is a very attractive choice for sensing applications due to the fact that it is a common path interferometer, that is, the reference arm (for the light reflected off the fixed mirrors) and the measurement arm (for the light reflected off the movable mirrors) almost share the same optical path except for the small mirror gap d . Hence, external disturbances are identical in both arms, which results in cancellation and stable interference signals. Sensors constructed

using common path interferometers usually tend to have higher signal-to-noise ratios (SNR) compared with those based on non-common path interferometers such as Michelson interferometers.

Lamellar grating interferometers can also be used in FTIR spectrometers [116]. In this case, the zeroth-order diffracted beam from the grating is recorded as the interferogram $I(\delta)$ while the movable mirrors move a sufficient amount to scan the OPD. The spectrum of the light source is again obtained through a Fourier transformation of the interferogram using Equation 1.20. In fact, a lamellar grating interferometer has a number of outstanding advantages for FTIR, including the absence of beam splitters, extended wavelength range, robustness (common-path interferometer), and high efficiency.

Again, lamellar grating interferometers based on optical MEMS can be built in two ways, namely out-of-plane and in-plane configurations. Figure 1.25b shows a micromachined biosensor using a lamellar grating interferometer in an out-of-plane configuration [117,118]. As shown, the sensor consists of a pair of suspended silicon nitride micro cantilevers, with one having a functionalized surface with receptors that are specific to the ligand under detection and the other without functionalization serving as a reference. At the tips of the cantilevers, interdigitated fingers are attached to act as the movable and fixed mirrors thus forming the lamellar grating interferometer. The interferometer is illuminated with a laser beam and the first-order diffraction is monitored. The presence of the ligand under detection bends the sensing cantilever thus creating a gap between the interdigitated fingers, inducing an OPD, and varying the intensity of the selected diffraction order. Figure 1.25c shows an optical MEMS gyroscope based on an out-of-plane lamellar grating interferometer [119]. As shown, the two proof masses are driven into in-plane anti-phase oscillations along a direction parallel to the device substrate with the same frequency. Interdigitated finger-like mirrors are also integrated on the two masses forming a lamellar grating interferometer. When the device experiences a rotation about an axis as indicated in the figure, the Coriolis forces on the two proof masses are also anti-phase, that is, pulling down one and pushing up the other. This creates a separation gap between the two sets of mirrors that is proportional to the rate of rotation. This dynamically changing gap is then detected by illuminating the interferometer with a laser beam and monitoring its diffraction orders. There are a number of sensors built on the basis of such out-of-plane configured lamellar grating interferometers, which include nano-g resolution accelerometers [120,121], electromagnetically-driven lamellar grating FTIR spectrometers [122], AFM cantilevers [123], and many others.

Figure 1.25d illustrates an example of a lamellar grating interferometer in an in-plane configuration [115]. The interferometer is developed using SOI microfabrication technology and designed for use as an FTIR spectrometer. As shown, deep-etched silicon side walls in the device layer of an SOI wafer are used as mirrors with one set anchored to the substrate and the other movable set attached to a MEMS electrostatic comb drive. The spectrometer can scan an OPD of about 145 μm resulting in a spectral resolution of a few nanometres in the visible spectrum range.

1.5.2.3 Optical MEMS sensors based on Fabry–Pérot interferometers

A Fabry–Pérot interferometer or cavity is another well-known interferometer commonly used in optical MEMS sensors. As shown in Figure 1.26a, the interferometer consists of two parallel mirrors separated with a gap d . The mirrors are identical and lossless with reflectance R . The overall coefficients of transmission (T_{FP}) and reflection (R_{FP}) of the system can be expressed as follows [124]:

$$T_{FP} = \frac{(1-R)^2}{(1-R)^2 + 4R \sin^2\left(\frac{\delta}{2}\right)}, \quad (1.24)$$

$$R_{FP} = \frac{4R \sin^2 \delta}{(1-R)^2 + 4R \sin^2\left(\frac{\delta}{2}\right)}, \quad (1.25)$$

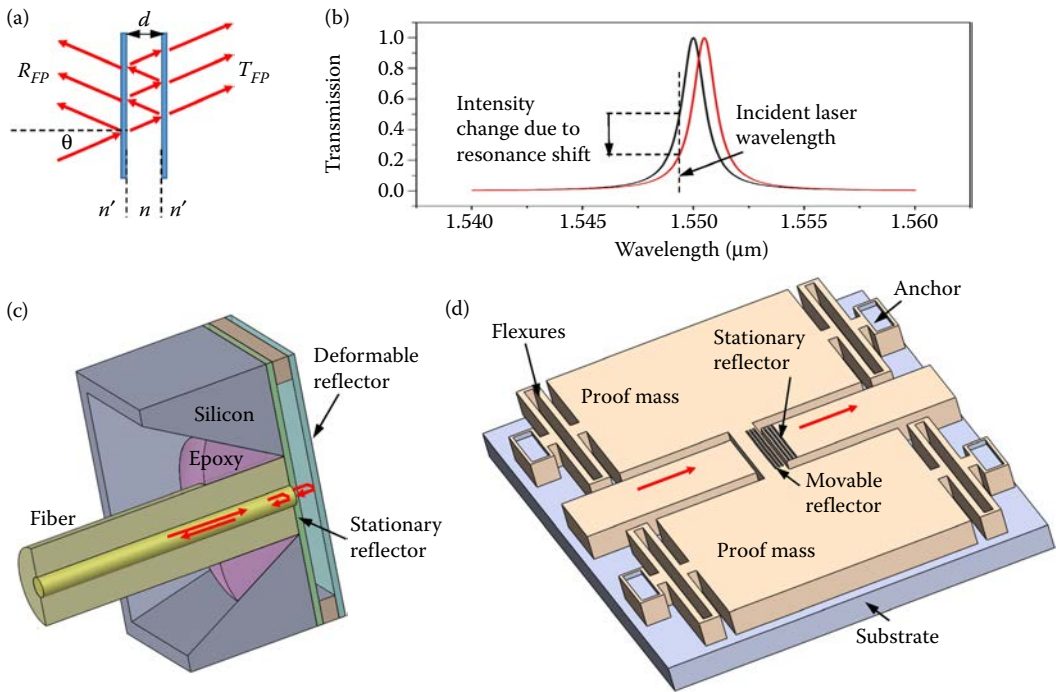


Figure 1.26 (a) Operation principle of a Fabry–Pérot interferometer, (b) typical optical readout mechanisms for sensors based on Fabry–Pérot interferometers, (c) a fiber-end-based Fabry–Pérot interferometric sensor, and (d) an in-plane constructed Fabry–Pérot interferometer for acceleration sensing.

where $\delta = (4\pi nd/\lambda) \cos(\theta)$ is the round-trip phase difference. When the resonant conditions, that is, $\delta = 2k\pi$ (k is an integer), are met, the transmission and reflection spectra show, respectively, a strong peak and a dip. The higher the reflectance of the mirror R , the sharper the transmission peak and reflection dip.

Both the reflection and transmission from a Fabry–Pérot interferometer can be used for sensing, and normal incidence ($\theta = 0^\circ$) is usually utilized. As an example, Figure 1.26b shows the transmission coefficient of the interferometer as a function of wavelength λ . Here, we assume normal incidence, the mirror reflectance $R = 0.98$, and the medium between the two mirrors is air ($n = 1$). The black and red curves show, respectively, the transmission spectra when the mirror gap d is at 6.2 and 6.21 μm , that is, when there is an increase of about 10 nm. It is quite clear that the sensors built on the Fabry–Pérot interferometers can be very sensitive owing to the fact that even a minute gap change can induce a drastic shift in the resonance transmission peak. Two detection methods are commonly used to obtain the minute gap variation from the interference signal. The first one is to directly track the wavelength shift of the resonant peak with a spectrometer [125]. The second method is to lock the incident laser beam to the half-maximum of the initial resonance peak (or a quadrature point) and monitor the output laser intensity from the interferometer [126]. As shown in the figure, the resonance shift due to the cavity gap change induces a large laser intensity variation. The latter has a number of advantages including high sensitivity and fast signal response, however, its dynamic sensing range is limited.

A majority of the sensors based on Fabry–Pérot interferometers are constructed in an out-of-plane configuration due to the high-quality mirror surfaces. A large number of sensors are demonstrated including pressure [127], acoustic and ultrasound [128–130], temperature [131], and chemical detectors [126]. Some are the stand-alone types with integrated photodetectors [126], and some are integrated with optical fibers for light input and output as shown in Figure 1.26c. For the fiber-based type, the movable reflector can be micromachined membranes coated with high-reflective coatings, high contrast gratings [132], or photonic crystal mirrors [133]. The stationary mirror can

be fabricated on the substrate or directly coated on the fiber end face. The fiber and machined chip are usually aligned and fixed with epoxy. The measurand to be detected changes the gap between two mirrors thereby affecting the sensor output. There are also optical MEMS sensors reported based on Fabry–Pérot interferometers in an in-plane configuration including chemical sensors [134] and accelerometers [135]. The latter is illustrated schematically in Figure 1.26d. It is fabricated in a thick device layer on an SOI wafer. As shown, the two distributed Bragg reflectors (DBR) are formed by etching air slots in silicon structures. The accelerometer is constructed by fixing one DBR and attaching the other to a suspended proof mass. Transmission of the Fabry–Pérot interferometer is monitored by guiding the light in and out using a silicon waveguide.

1.6 Conclusions

Optical MEMS devices that integrate MEMS with optics at the micro scale have shown great potential in sensing, imaging, and communication. In this chapter, we have briefly review the MEMS technology, actuation mechanisms, and their applications in sensing, imaging, and display. Other optical MEMS devices and systems that are equally important but are less covered in this chapter include optical switches, variable attenuators, tunable lasers, tunable lenses and apertures, deformable mirrors, and many others. Many optical MEMS devices including TI's DLP are already in the market, others are rapidly developing in various research laboratories. The future of optical MEMS seems bright.

References

1. O. Brand, Fabrication Technology, in *CMOS—MEMS*, Wiley-VCH Verlag GmbH, by O. Brand, G.K. Fedder (Eds.), Weinheim, Germany, pp. 1–67, 2008.
2. V. Saile, H. H. Gatzert, J. Leuthold, *Micro and Nano Fabrication Tools and Processes*, Springer, Berlin, 2013.
3. F. Laermer and A. Schilp, Method of Anisotropic Etching of Silicon, US Patent, 2003.
4. J. A. Dziuban, *Bonding in Microsystem Technology*, Springer, Netherlands, 2006.
5. D. J. Bell, T. Lu, N. A. Fleck, and S. M. Spearing, MEMS actuators and sensors: Observations on their performance and selection for purpose, *Journal of Micromechanics and Microengineering*, vol. 15, p. S153, 2005.
6. A. Jain, H. Qu, S. Todd, and H. Xie, A thermal bimorph micromirror with large bi-directional and vertical actuation, *Sensors and Actuators A: Physical*, vol. 122, pp. 9–15, 2005.
7. S. T. Todd and H. Xie, An electrothermomechanical lumped element model of an electrothermal bimorph actuator, *Journal of Microelectromechanical Systems*, vol. 17, pp. 213–225, 2008.
8. J. Sun, S. Guo, L. Wu, L. Liu, S.-W. Choe, B. S. Sorg et al., 3D *in vivo* optical coherence tomography based on a low-voltage, large-scan-range 2D MEMS mirror, *Optics Express*, vol. 18, pp. 12065–12075, 2010.
9. S. Pal and H. Xie, Analysis and fabrication of curved multimorph transducers that undergo bending and twisting, *Journal of Microelectromechanical Systems*, vol. 21, pp. 1241–1251, 2012.
10. J. H. Comtois and V. M. Bright, Applications for surface-micromachined polysilicon thermal actuators and arrays, *Sensors and Actuators A: Physical*, vol. 58, pp. 19–25, 1997.
11. L. Li and D. Uttamchandani, Modified asymmetric micro-electrothermal actuator: Analysis and experimentation, *Journal of Micromechanics and Microengineering*, vol. 14, p. 1734, 2004.
12. H. Veladi, R. Syms, and H. Zou, A single-sided process for differentially cooled electrothermal micro-actuators, *Journal of Micromechanics and Microengineering*, vol. 18, p. 055033, 2008.